



# Subduction plate interface shear stress associated with rapid subduction at deep slow earthquake depths: example from the Sanbagawa belt, Southwest Japan

Yukinojo Koyama<sup>1</sup>, Simon R. Wallis<sup>1</sup>, Takayoshi Nagaya<sup>2</sup>

5 <sup>1</sup>Department of Earth and Planetary Science, The University of Tokyo, Tokyo, 113-0032, Japan

<sup>2</sup>Department of Environmental Science, Tokyo Gakugei University, Tokyo, 184-8501, Japan

**Correspondence to:** Yukinojo Koyama ([koyamanojo@g.ecc.u-tokyo.ac.jp](mailto:koyamanojo@g.ecc.u-tokyo.ac.jp)), Simon R. Wallis ([swallis@eps.s.u-tokyo.ac.jp](mailto:swallis@eps.s.u-tokyo.ac.jp)), Takayoshi Nagaya ([tnagaya@u-gakugei.ac.jp](mailto:tnagaya@u-gakugei.ac.jp))

10 **Abstract.** Absolute maximum shear stress (“shear stress” in this study) along the subduction plate interface is important for understanding earthquake phenomena and is an important input parameter in subduction zone thermomechanical modelling. However, such shear stress is difficult to measure directly at depths more than a few kilometers and is generally estimated by simulation using a range of input parameters with large associated uncertainties. In addition, estimated values generally represent shear stress conditions over short observation timescales, which may not be directly applicable to long-timescale  
15 subduction zone modelling. Rocks originally located deep in subduction zones can record information about deformation processes, such as shear stress conditions, occurring in regions that cannot be directly accessed. The estimated shear stress is likely to be representative of shear stress experienced over geological timescales and be suitable to use in subduction zone modelling over time scales of millions to tens of millions of years. In this study, we estimated shear stress along a subduction plate interface by using samples from the Sanbagawa metamorphic belt of Southwest (SW) Japan, in which slivers of mantle  
20 wedge-derived serpentinite are widely distributed and in direct contact with metasedimentary rocks derived from the subducted oceanic plate. These areas can be related to the ancient subduction plate interface.

To obtain estimates of shear stress at the subduction interface, we focused on the microstructure of quartz-rich metamorphic rocks—quartz is the main component of the rocks we collected and its deformation stress is assumed to be representative of the region. Shear stress was calculated by applying deformation temperatures estimated by the crystallographic orientation of  
25 quartz (the quartz c-axis fabric opening-angle thermometer), and the apparent grain size of dynamically recrystallized quartz in a thin section to an appropriate piezometer. Combined with information on sample deformation depth, estimated from P–T path and deformation temperatures, it is suggested that there was nearly constant shear stress of 16–41 MPa in the depth range 17–27 km, assuming plane stress conditions even when uncertainties related to measurement direction of thin section and piezometer differences are included.

30 The Sanbagawa belt formed in a warm subduction zone. Deep slow earthquakes are commonly observed in modern-day warm subduction zones such as SW Japan, which has a similar thermal structure to the Sanbagawa belt. In addition, deep slow earthquakes are commonly observed to be concentrated in a domain under the shallow part of the mantle wedge. Samples showed the depth conditions near the mantle wedge, suggesting that these samples were formed in a region with features



similar to the deep slow earthquakes domain. Estimated shear stress may not only be useful to long-timescale subduction zone  
35 modelling but also represent the initial conditions from which slow earthquakes in the same domain nucleated.

## 1 Introduction

Knowledge about the distribution and values of absolute maximum shear stress (“shear stress” in this study) along the  
subduction plate interface is fundamental to understanding seismic phenomena and the thermal evolution of subduction zones:  
earthquakes along the plate interface occur when the shear stress on a fault plane exceeds the shear strength (e.g., Vavryčuk,  
40 2015), and frictional heating increases with increasing shear stress, which can significantly affect the thermal structure of  
subduction zones (e.g., Ishii and Wallis, 2020). Recently, it has also been suggested that for the same material and fault plane,  
the initial shear stress values significantly affect slip rates, rupture rates, and stress drop values (Passelègue et al., 2020).

However, direct measurement of shear stress at plate interfaces is difficult and the associated strength along the subduction  
plate interface is not well known. Estimates of shear stress can be obtained by direct measurement of borehole breakouts and  
45 drilling-induced tensile fractures (e.g., Chang et al., 2010; Lin, 2014). However, such techniques are limited to relatively  
shallow areas with depths of up to a few kilometers. At greater depths, friction coefficients (shear strength) and shear stress  
have been estimated from subduction plate interface simulation using surface heat flow, friction law, and flow law combined  
with thermal modeling (e.g., Gao and Wang, 2014; England, 2018). A difficulty encountered when using surface heat flow is  
its strong local scatter due to bottom water temperature variations, the influence of localized fluid flow, and other upper crustal  
50 processes (e.g., Gao and Wang, 2014; England, 2018; Ishii and Wallis, 2020). As an example, Gao and Wang (2014) modelled  
shear stress along the Kamchatka subduction plate interface and concluded that the average effective coefficient of friction lies  
within the range 0.03–0.09 with the uncertainties largely due to the large scatter in the heat flow values related to variations in  
bottom water temperature. The uncertainties yield a correspondingly large range in estimates for the maximum estimated shear  
stress is about double the minimum estimated value (Fig. S4 in Gao and Wang, 2014). In addition, features such as the thickness  
55 of the actively deforming plate interface and the parameters that make up the flow law are generally not well constrained and  
these also affect the results. These issues can lead to order of magnitude uncertainties in estimates of shear stress and strength.  
Stress inversion using seismic data has also been used to estimate the strength of the subduction boundary and the surrounding  
crust (e.g., Yoshida et al., 2015). However, this approach is limited to the brittle deformation domain and it is difficult to obtain  
values for absolute stress. A further issue is that any stresses obtained from the above approaches are only representative of  
60 the observation period. When stresses are used in a model, ideally, they should be estimated on a time scale appropriate for  
the phenomenon being examined. However, the time scales of observation and the modelled phenomena are commonly very  
different. For instance, stresses estimated from seismic data represent several orders of magnitude shorter time scales than the  
thermal evolution of a subduction zone which develops over time scales of millions to several tens of millions of years.

The study of rocks that were once distributed along the plate interface is one of the key ways to obtain information along  
65 deeper inaccessible parts of subduction zones. The most reliable and widely used differential (shear) stress indicator in such



rocks is based on grain size measurements and this technique is referred to as piezometry (e.g., Twiss, 1977; Twiss, 1980; Derby, 1991; Stipp and Tullis, 2003; Shimizu, 2008; Shimizu, 2012; Cross et al., 2017; Goddard et al., 2020). The relationships used in such piezometry express the dynamically recrystallized grain size of a particular mineral as a function of deformation temperature and applied differential stress. Differential stress is the cause of non-volumetric strain and is defined as the difference between the greatest and least principal stress. Shear stress is equal to half the differential stress. Most piezometers are calibrated based on deformation experiments that use uniaxial compressive stress states. However, most naturally deformed rocks show approximately plane strain suggesting deformation under plane stress conditions. Shear stress required to deform a material under uniaxial conditions can be converted to the shear stress required under plane stress conditions using properties of the deviatoric stress tensor (see Appendix B).

70 Taking a broad range in possible widths for the subduction channel of 100 m–10 km, and a representative subduction rate of 3 cm per year due to plate motion causing simple shear throughout the subduction channel, the calculated strain rate is  $10^{-13}$ – $10^{-11}$  s<sup>-1</sup>. Dynamic recrystallization requires strains of at least 0.2 (e.g., Stipp and Tullis, 2003). In this situation, the time required for dynamic recrystallization is about 0.01–1 million years. Therefore, obtained stress values can be regarded as representative of the stress state over a period of at least 0.01–1 million years and are more appropriate for considering the geological timescale evolution of subduction zones compared with stress values obtained by drilling or thermal observations.

80 In this study, we applied piezometers to dynamically recrystallized quartz grains observed in rocks of the subduction-type Sanbagawa belt in SW Japan to estimate differential (shear) stress along the subduction zone plate interface. In the Sanbagawa belt, slivers and blocks of mantle wedge-derived serpentinite are widely distributed and in direct contact with sedimentary rocks derived from the subducted oceanic plate. These areas can be related to an ancient subduction plate interface (Aoya et al., 2013a). We found that there was no clear correlation between the deformation depth and differential (shear) stress in the depth range of 17–27 km along the subduction zone plate interface, and differential (shear) stress at this depth range was almost constant. This result contrasts with a previous study (Takeshita, 2021), which proposes a trend of decreasing differential stress with increasing metamorphic temperature and pressure. This difference may be due to the fact that Takeshita (2021) did not consider the temperature dependence in the piezometer. This temperature dependence reflects a balance between recrystallized grain nucleation and migration of grain boundaries. We estimated deformation temperatures using an empirical relationship between quartz c-axes orientation patterns and deformation temperatures, and selected samples appropriate for discussions of the deformation on the subduction plate interface. In this study, we focus on the relationship between the differential (and shear) stress and the stress state along the subduction plate interface. This is also in contrast to Takeshita (2021) who focuses on the relationship between the obtained stress values and exhumation processes.

90 Our study shows that the Sanbagawa belt is not only useful to long-timescale subduction zone modelling but also suitable to study deep slow earthquakes and the estimated differential (shear) stress likely represents the initial conditions under which slow earthquakes in the same domain nucleated.



## 2 Method

### 2.1 The Sanbagawa belt

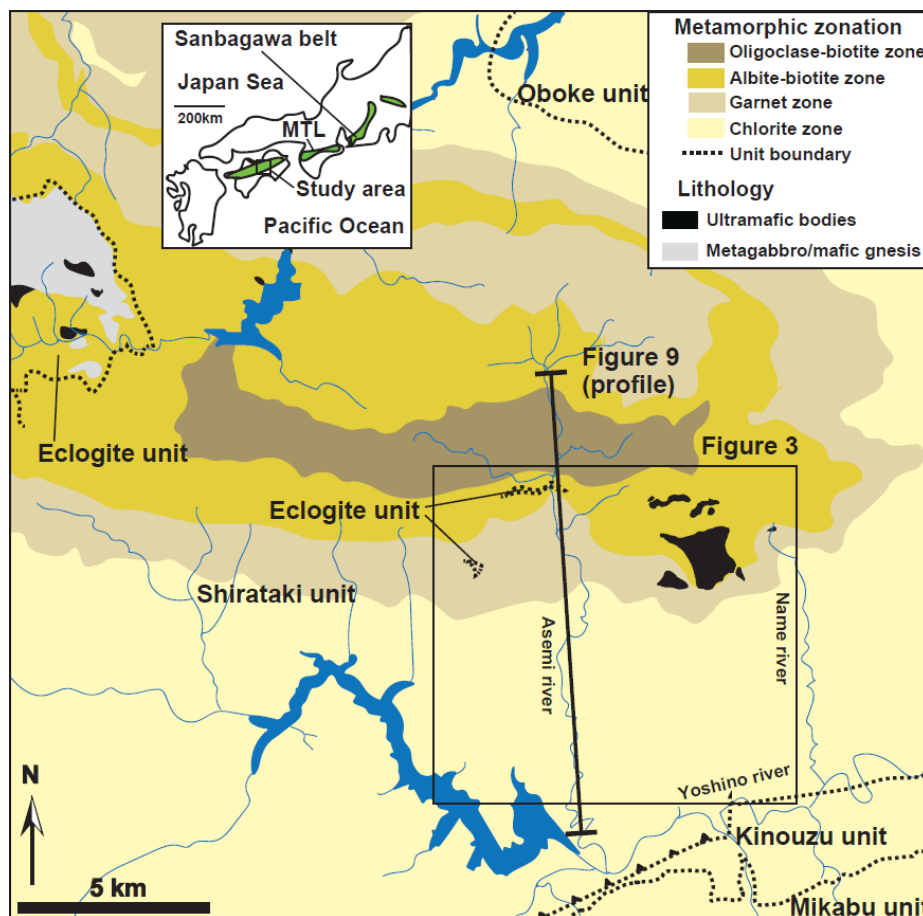
100 The Sanbagawa belt is a belt of high-P subduction-type metamorphism developed in the eastern Asian convergent margin during the Cretaceous (Isozaki and Itaya, 1990; Wallis et al., 2009) and is now exposed over a distance of about 800 km from east to west in Southwest (SW) Japan. The widest range of metamorphic conditions is shown by rocks in central Shikoku and this area was chosen for more detailed study (Fig. 1). The Sanbagawa belt is bounded to the north by a major tectonic discontinuity, the Median Tectonic Line (MTL) and in central Shikoku the southern boundary of the Sanbagawa belt is marked  
105 by the presence of significantly older units (the Kinouzu and Mikabu units) which have undergone the Sanbagawa metamorphism but represent a tectonically distinct structurally overlying domain and interpreted as part of the original hanging wall to the Sanbagawa subduction complex (Endo and Wallis, 2017).

Three distinct geological units can be defined within the Sanbagawa belt of central Shikoku. The Eclogite unit is located at the highest structural level (Aoya et al., 2013a) and underwent eclogite facies metamorphism at 89–88 Ma (Wallis et al., 2009).  
110 Parts of this unit are distinctly coarser grained and show early Cretaceous (about 120 Ma) metamorphic ages (Okamoto et al., 2004; Endo et al., 2009). The Shirataki unit, the subject of this study, structurally underlies the eclogite unit. Buoyancy-driven rise of the eclogite unit within the subduction boundary domain is thought to have emplaced it above the Shirataki unit (Aoya, 2001; Endo et al., 2012; Aoya and Endo, 2017). After the amalgamation of the Eclogite and Shirataki units, they both underwent a distinct phase of metamorphism at 89–85 Ma (Endo et al., 2012), which overprints the eclogite metamorphism  
115 and is referred to here as the main metamorphism. The Oboke unit represents the lowest structural level of the Sanbagawa metamorphic belt and consists dominantly of pelitic and psammitic schists. The Shirataki unit has been thrust over the Oboke unit (Wallis, 1998).

The main metamorphism is divided into four metamorphic grades (Fig. 1) based on constituent minerals in metapelite (Higashino, 1990). In order of increasing grade and their estimated peak metamorphic T and P, these zones are: the chlorite  
120 zone (<360°C, 0.5–0.6 GPa); garnet zone (440±15°C, 0.7–0.8 GPa); albite-biotite zone (520±25°C, 0.8–0.9 GPa); and oligoclase-biotite zone (610±20°C, 0.9–1.1 GPa) (Enami et al., 1994; Fig. 2a). The metamorphic zones are generally E–W oriented, with the highest metamorphic temperature and pressure conditions generally found at the highest structural levels. In central Shikoku, the isograds have been tightly folded (e.g., Wallis et al., 1992; Mori and Wallis, 2010; Kouketsu et al., 2021), and the highest-grade units are locally found at intermediate structural levels, from which the temperature and pressure  
125 conditions decrease both to the north and south (Fig. 1). This recumbent folding formed by deformation after the peak of the main metamorphism is referred to as D<sub>s</sub> following Wallis (1990) and is described in more detail below.

### 2.2 Deformation of Shirataki unit during the main metamorphism

In this study, our main focus is the ductile deformation in the Shirataki unit. The Shirataki unit is composed of subducted oceanic crust with basalt, chert, sandstone, and mudstone metamorphosed into basic (mafic), quartz, psammitic, and pelitic



130

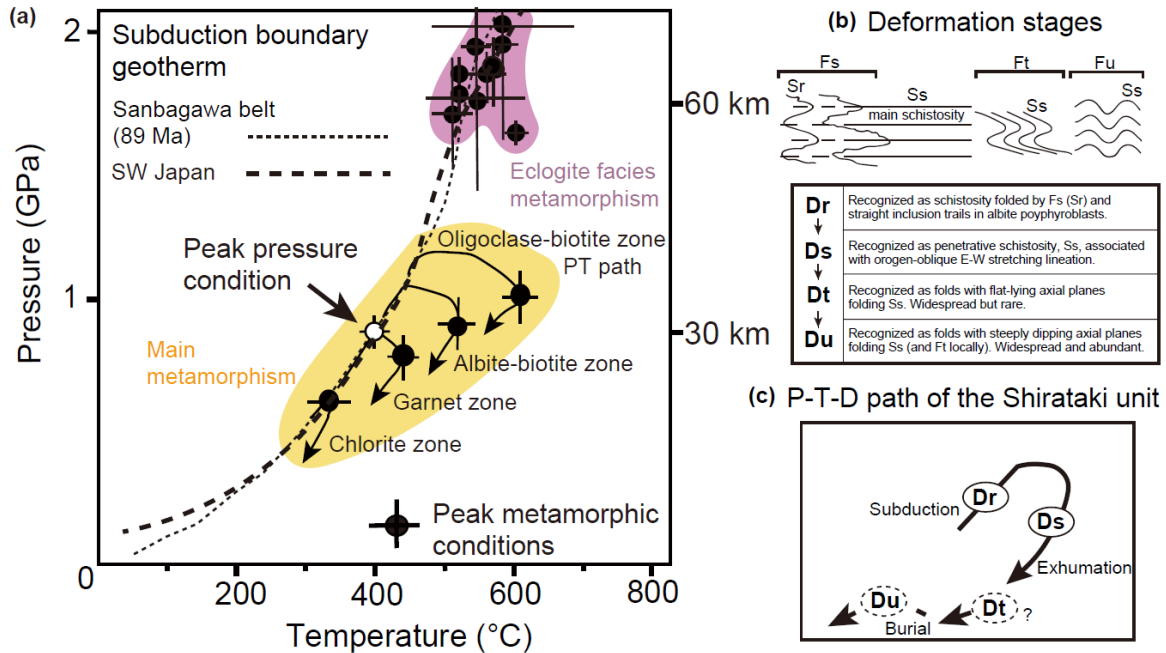
**Figure 1: Location, geological units, and metamorphic zonation map of the Sanbagawa metamorphic belt in central Shikoku (after Kouketsu et al., 2021; Aoya et al., 2013b; Endo et al., 2018; Higashino, 1990).**

135

types of schist (Mori & Wallis, 2010; Fig. 3). There are also rare but widely dispersed ultramafic bodies derived from the mantle wedge (Fig. 3).

140

The main metamorphism that formed the Shirataki unit has four recognized ductile deformation phases, named Dr, Ds, Dt, and Du deformation, respectively (Wallis, 1990; Fig. 2b, 2c). Dr deformation is locally the main deformation phase particularly in the high temperature-pressure zone (i.e., oligoclase-biotite zone), but in most cases, major deformation structures are due to Ds deformation, and Dr deformation is preserved mainly as inclusion trails in albite porphyroblasts representing a Sr foliation (Mori and Wallis, 2010) which has been strongly overprinted. Compositional zoning of amphibole in and outside the porphyroblasts indicates that the Dr deformation was formed during the subduction, burial phase (Wallis et al., 1992). The Ds deformation is characterized by an overall gently north-dipping Ss foliation, and a generally WNW–ESE oriented stretching direction (Aoya et al., 2013b; D1 and D2 deformation in Banno & Sakai, 1989; L1 lineation in Faure, 1985), which is highly oblique to the distribution of the Sanbagawa belt. The Ds deformation is considered to have occurred close to or shortly after



145

**Figure 2: (a) Petrographically derived P–T conditions of the Sanbagawa metamorphic belt (black and white circles). The thin dashed line represents subduction-boundary geotherm at c. 89 Ma from P–T estimates (Aoya & Endo, 2017; Aoya et al., 2017). The bold dashed line represents the inferred subduction-boundary geotherm for modern day SW Japan based on thermal modelling by Yoshioka and Murakami (2007) (b) Summary of deformation stages and their associated structures in the Shirataki unit based on Wallis et al. (1992) and Aoya (2001, 2002) modified by Kouketsu et al. (2021). (c) Main metamorphism P–T–D path of the Shirataki unit (Aoya, 2001) modified by Kouketsu et al. (2021).**

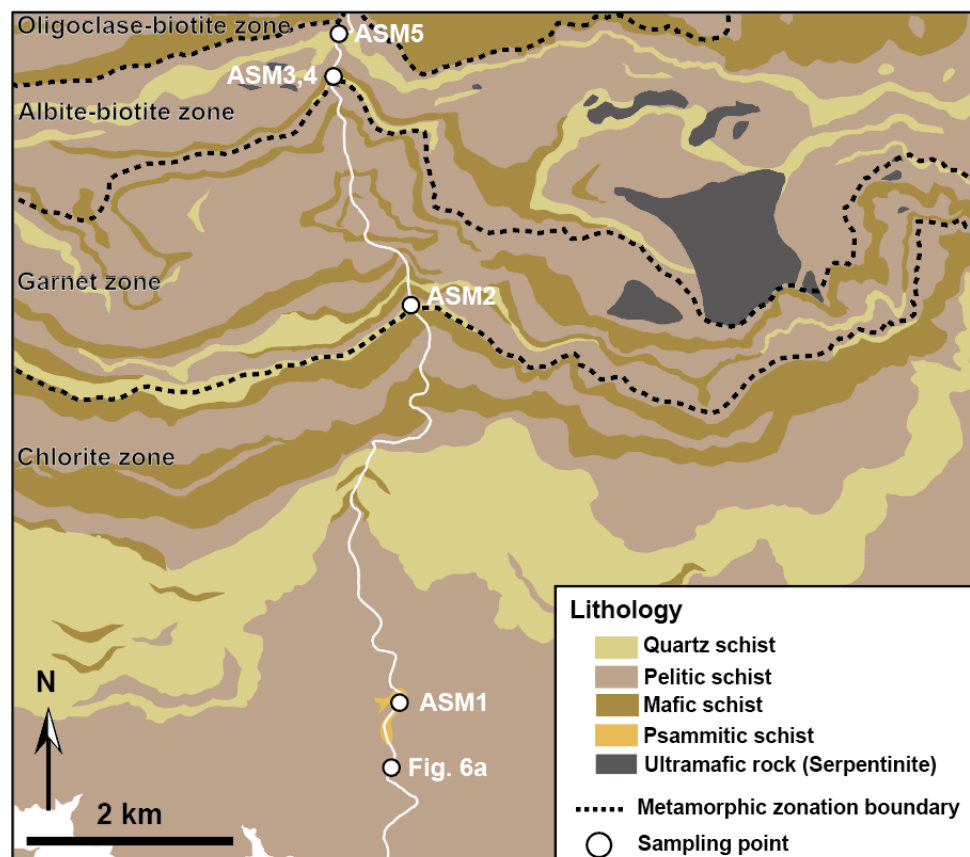
150

the peak temperature condition because metamorphic isograd surfaces were folded in this phase (including the recumbent fold described above). However, compositional changes of amphibole in the porphyroblasts and of Na-pyroxene in equilibrium with albite of the garnet zone suggest that part of the Ds deformation occurred during a pressure drop and temperature increase, i.e., before the peak metamorphic temperature was reached (Wallis et al., 1992; Enami et al., 1994). Dt and Du deformation are identified where the Ss foliation is folded (Wallis et al., 1992). Both structures have E–W oriented fold axes, but the Dt deformation is distinguished by axial surfaces that dip gently to the north, while the Du deformation is distinguished by fold axial surfaces that are nearly vertical (Wallis, 1990; D3 folds in Banno and Sakai, 1989).

155

160

As mentioned above, when the Ds deformation occurred, the Sanbagawa belt was exhuming. However, the orogen-oblique stretching lineation of the Ds deformation is thought to reflect deformation closely related to rapid (24 cm/yr: Engebretson et al., 1985; Ishii & Wallis, 2020) and oblique subduction of the subducted Izanagi Plate (e.g., Wallis, 1992; Wallis et al., 2009). In addition, Ds structures are also the most widely developed in the Sanbagawa belt. Therefore, this study focuses on the deformation structures associated with Ds deformation to discuss the deformation along the subduction plate interface.



165

Figure 3: Geological map (after Endo and Yokoyama, 2019), metamorphic zonation, and sampling points of this study.

### 2.3 Sampling and preparation for analysis

Five samples were collected at four locations to obtain deformation information under a wide range of temperature and pressure conditions (Fig. 3: ASM1–5). ASM1 is a sample from deformed quartz veins, which are in psammitic schist and are oriented subparallel to the foliation, and samples ASM2–5 are from quartz schist. Samples strongly affected by Dt or Du deformation were not used in this study.

The orientations of the Z-axes of finite strain were taken to be normal to the Ds foliation. The orientations of the X- and Y-axes were taken to lie within the Ds foliation, the X-axes were taken to be parallel to the Ds stretching lineation, and the Y-axes were taken to be perpendicular to the Ds stretching direction. Thin sections were prepared from chips cut parallel to the Z-axis and polished using a series of alundum types with decreasing grain sizes of #180 (about 80  $\mu\text{m}$ ), #320 (about 50  $\mu\text{m}$ ), #800 (about 20  $\mu\text{m}$ ), #2000 (about 7.5  $\mu\text{m}$ ), #3000 (about 5  $\mu\text{m}$ ) and a series of diamond pastes with grain sizes of 3, 1, and 1/4  $\mu\text{m}$ . After this sequence of polishing, the thin sections were further treated with colloidal silica to remove the surface

175



180 damage zone before they were suitable for electron backscatter diffraction (EBSD) measurements as discussed below. Each phase of polishing took 30–120 minutes, which depends on the surface condition of the thin section.

## 2.4 Differential (shear) stress estimation

We estimated the differential (shear) stress using piezometers based on the recrystallized grain size of quartz, which is the dominant mineral phase of the rocks examined. The following points were noted in the grain size measurements.

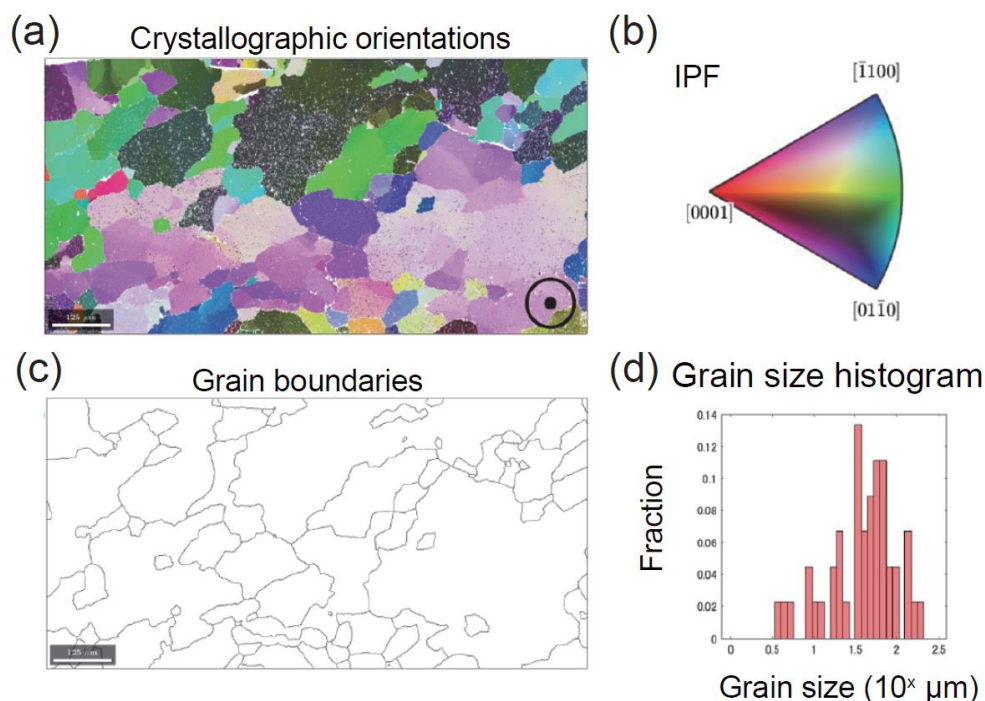
- 185 1. Quartz-only domains were selected for analysis to remove the effects of grain growth inhibition by the presence of other minerals such as mica. In the thin sections used for the measurements, changes in grain size due to grain growth inhibition caused by the presence of other minerals was observed. When quartz-rich domains were compared there was no clear changes within a single thin section and the calculated grain size can be considered to be representative at least of the grain size in the thin section.
- 190 2. The general presence of well-developed foliation and stretching lineation in the region suggests that samples and selected microstructural domains deformed under conditions close to plane strain. To examine any potential sectioning effects, the grain size for individual samples was measured in both the XZ and YZ planes and treated as maximum and minimum grain sizes. When the Ds lineation is not well developed, the grain size was measured using a thin section oriented parallel to the Z-axis (PZ plane).

Grain size measurements of the samples were performed using W–SEM–EBSD and open-source MTEX toolbox for MATLAB  
195 (<http://mtex-toolbox.github.io/>). Crystallographic orientations were determined using W–SEM equipped with an EBSD system (JEOL JSM-6510LV with Oxford HKL Channel5) at the University of Tokyo. In the W–SEM, the load current was 73–107  $\mu$ A. The W–SEM magnification during observation and measurement was kept to  $\times 40$ . A step size of 1  $\mu$ m was used for mapping. HKL database from Sands (1969) was used for the quartz EBSD indexing. Other analytical conditions followed Nagaya et al. (2022). The grain boundaries were constructed from EBSD crystallographic orientation data using a Voronoi  
200 decomposition algorithm (Bachmann et al., 2011) implemented within the MTEX toolbox, and grain size distribution was calculated by measuring the area of each grain and converting it to the diameter of a circle with the same area (Fig. 4). A Matlab script provided by Cross et al. (2017) was used in the analysis; this script defines grain boundaries where the misorientation angle is  $>10^\circ$  and RMS grain size is used to represent the average grain size.

205 Recrystallized grains in natural rocks can be produced by three mechanisms: bulging (BLG), subgrain rotation (SGR), and grain boundary migration (GBM or a combination of SGR+GBM) (Stipp et al., 2002; Shimizu, 2008). BLG and SGR form new dynamically recrystallized grains; GBM is a mechanism where energetically stable particles consume unstable particles by grain boundary migration.

Recrystallized grains formed by BLG or SGR are derived from initial usually larger grains and some of these grains may still be present in the microstructure. To apply the piezometer selected in this study it is necessary to filter these relict grains. This  
210 filtering was performed following the method of Cross et al. (2017). The grain size was then calculated and applied to “EBSD 1  $\mu$ m RMS piezometer” of Cross et al. (2017) to estimate differential (shear) stress, which is the empirical relationship between





215 **Figure 4: Summary of the method used to determine grain boundaries and grain size distribution. (a) Crystallographic orientations measured by W-SEM-EBSD (Inverse pole figure map) and (b) the corresponding inverse pole figure.  $\odot$  shows the observation direction of the crystallographic orientation (perpendicular to the paper). [0001] indicates the direction of the c-axis. (c) Grain boundaries were determined using a critical misorientation angle. Grains that did not interest the map border were used for the grain size calculation. (d) Grain size distribution derived from image (c).**

the Root mean square (RMS) grain size formed by BLG or SGR and applied differential stress. Uncertainties of estimated differential (shear) stress are related to both the piezometer and the grain size measurement (Appendix C). In this study, the same procedure was also applied to microstructures formed by SGR+GBM. These grains filtered by Cross et al. (2017) are relatively unaffected by GBM and can be regarded as formed by SGR, indicating that the application of the Cross et al. (2017) piezometer is reasonable.

225 The domains consisting of recrystallized grains formed by SGR+GBM comprise a steady-state microstructure and are formed by one deformation stage. The type of microstructure is suitable for using the  $\alpha$ -quartz piezometer of Shimizu (2012), in which the relationship between the grain size of microstructures formed by SGR+GBM and applied differential stress is theoretically considered. To calculate grain size, the Matlab script provided by Cross et al. (2017) was revised following the definition of Shimizu (2012), in which boundaries where the misorientation angle is  $>12^\circ$  was used to define grain boundaries, and the mode of the logarithmic grain size was used to represent the grain size. No grain filtering was performed. The piezometer of Shimizu (2012) includes a temperature dependency, and deformation temperatures derived from quartz c-axes fabric opening-

230



angle thermometry (Sect. 2.5) was also applied. The uncertainties by the piezometer of Shimizu (2012) are not shown. Therefore, uncertainties of estimated differential (shear) stresses are only related to grain size measurement and deformation temperature (Appendix D).

## 2.5 Deformation temperature estimation by quartz c-axes fabric opening-angle thermometer

235 When the c-axis orientations of quartz aggregates deformed by high-strain dislocation creep are projected onto a stereonet, they commonly show strong preferred orientation patterns also known as fabric patterns. An opening-angle (OA) between the peripheral legs of such fabric patterns can be defined for many samples deformed at medium temperatures (Fig. 5). There is a nearly linear relationship between the OA of quartz fabrics formed by plane strain and the associated metamorphic temperatures estimated by petrological geothermometers from greenschist to granulite facies (Kruhl, 1998; Morgan and Law, 240 2004). In this study, the relationships presented in Fig. 2 of Law (2014) were used to estimate the deformation temperature. As with the data used in Law (2014), only quartz grains produced by dynamic recrystallization were used, and the 3D strain patterns were also classified. The relationships shown in Law (2014) indicate a 50° OA is equivalent to a deformation temperature of 400°C and a 1° increase/decrease in OA represents an 8°C increase/decrease in the deformation temperature. For the samples with a well-defined Ds stretching lineation, the c-axis orientations of quartz grains were obtained by W-SEM- 245 EBSD from thin sections parallel to XZ planes. When the Ds lineation is not observed in the sample, thin sections parallel to the Z axis (PZ plane) were used. Analytical conditions were the same as for the grain size determination, except the step size which was 5 μm for microstructures formed by SGR or SGR+GBM and 1 μm for microstructures formed by BLG. When analyzing microstructures formed by BLG or SGR, newly recrystallized grains were selected using the method of Cross et al. (2017), and the mean orientations of the c-axes of each selected grain were plotted in a Schmidt net. When 250 analyzing microstructures formed by SGR+GBM, all grains were plotted. Well-formed fabric patterns indicate that the selected grains were formed by a single deformation stage.

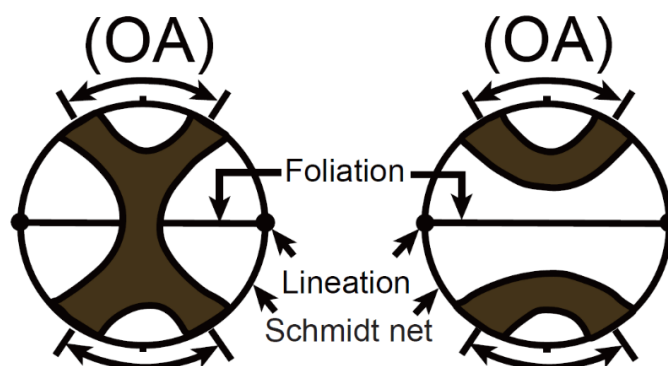


**Figure 5: Definition of OA. The dark regions correspond to high concentrations of quartz c-axes plotted on the Schmidt net. The left figure shows crossed girdle and the right figure shows a small girdle.**



### 255 3 Results

The  $D_s$  foliation and stretching lineation of psammitic and pelitic schist around sample ASM1 is defined by pressure solution seams and quartz strain fringes developed around pyrite observed in the surrounding area (Fig. 3; Fig. 6a). The orientation of the strain fringes shows an NWN–ESE oriented finite stretching and their asymmetry indicates a top to west shear sense, both consistent with the characteristics of  $D_s$  (Wallis, 1992). Sample ASM1 was collected from quartz veins oriented subparallel to  
260 the  $D_s$  foliation. Quartz grains in sample ASM1 are also elongated in an NWN–ESE direction, consistent with the characteristics of  $D_s$  deformation. These quartz grains exhibit wavy extinction, and some of them show segregation into multiple finer grains with homogeneous grain sizes (Fig. 6b). These microstructural features are evidence of dislocation creep and dynamic recrystallization by SGR (Stipp et al., 2002).

In sample ASM2, phyllosilicate minerals with a platy shape are strongly aligned and form a well-defined  $D_s$  foliation (Fig.  
265 6d). A thin section parallel to the foliation shows that quartz, phengite and opaque minerals are elongated or aligned defining a  $D_s$  mineral lineation (Fig. 6c). Quartz grains exhibit wavy extinction, amoeboid grain boundaries, and irregular grain sizes (Fig. 6d). These microstructural characteristics indicate the action of dislocation creep and dynamic recrystallization: GBM of Stipp et al. (2002) or SGR+GBM of Shimizu (2008).

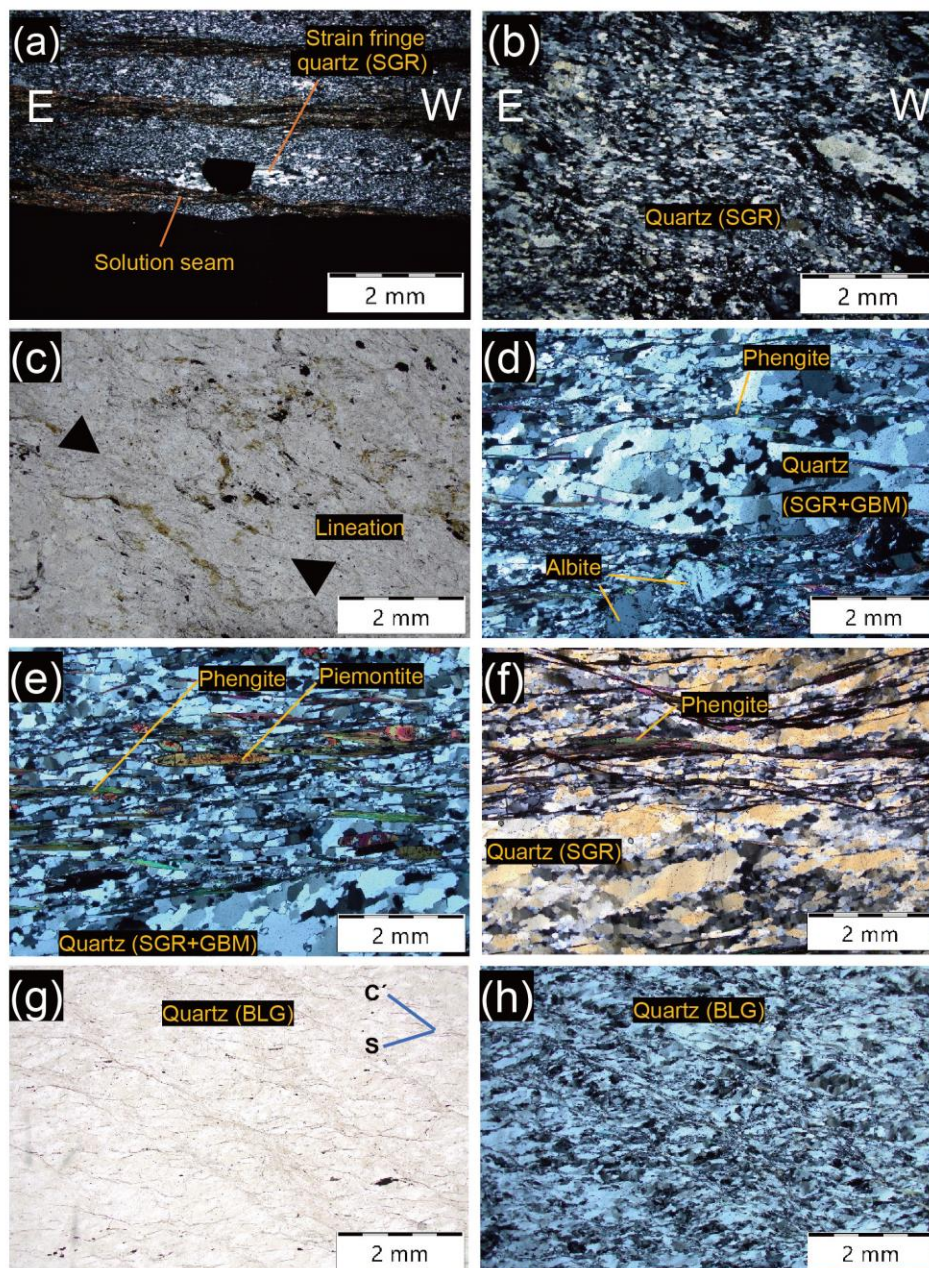
Samples ASM3 and 4 were collected from the albite-biotite zone. Phyllosilicate minerals are strongly aligned and form a  
270 well-defined  $D_s$  foliation (Fig. 6e, 6f). However, a clear lineation is not observed. Quartz grains exhibit microstructures characteristic of dislocation creep and dynamic recrystallization, ASM3 with SGR+GBM (Fig. 6e) and ASM4 with SGR (Fig. 6f).

Sample ASM5 was collected from the albite-biotite zone. In this sample, an  $SC'$  shear band structure is observed (Fig. 6g,  
6h). In the quartz domain wavy extinction is observed, and both bulges and recrystallized grains are present along grain  
275 boundaries. These microstructural characteristics indicate the action of dislocation creep and dynamic recrystallization: BLG of Stipp et al. (2002).

The results of observation and analyses are summarized in Table 1. Sample ASM2–5 showed a clear fabric pattern and an OA was measured (Fig. 7). Estimated deformation temperatures are shown in Table 2. Differential stress in both uniaxial and plane stress conditions (Appendix B) results are also listed in Table 3 (Uncertainties are shown in Fig. 10 and 12).

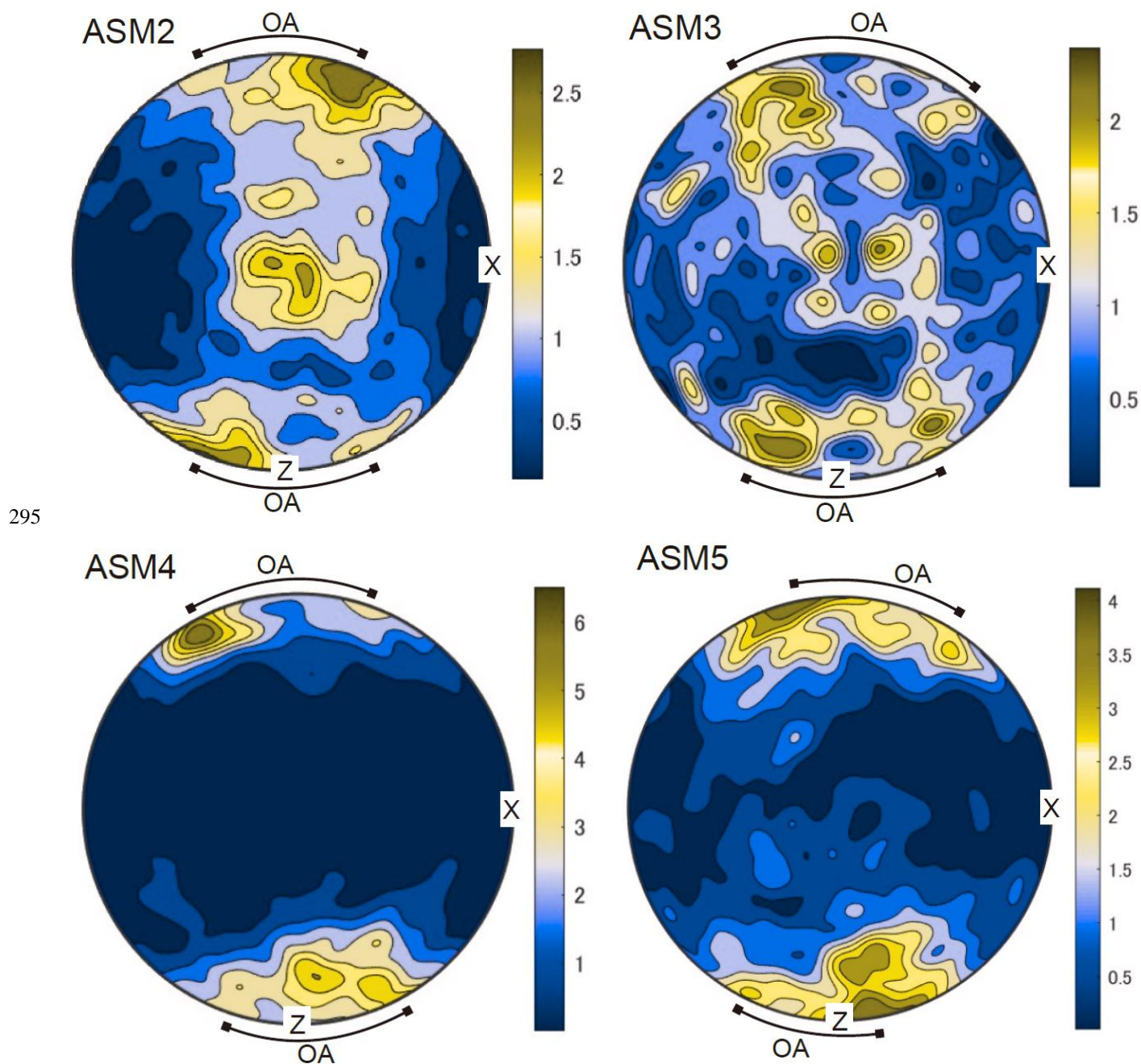
280

285



290

**Figure 6:** E and W indicate the eastern and western sides of the thin section. Except for (c) and (e), the up direction on the page corresponds to the up direction in the field. (a) Pelitic schist close to sample ASM1. XZ plane. Crossed nicols. (b) Sample ASM1. XZ plane. Crossed nicols. (c) Sample ASM2. XY plane. Opened nicols. Elongated phengite and quartz form weak lineation (arrow direction). (d) Sample ASM2 XZ plane. Crossed nicols. (e) Sample ASM3. PZ plane. Crossed nicols. (f) Sample ASM4. PZ plane. Crossed nicols. (g, h) Sample ASM5. PZ plane. (g) Opened nicols. (h) Crossed nicols.



300 **Figure 7: Collected quartz c-axis fabric pattern and measured OA. ASM2: 5001 grains; ASM3: 1840 grains; ASM4:**  
**2097 grains; ASM5: 1511 grains.**



**Table 1 Observation and analysis results**

Metamorphic zonation	Sample name	Mineral assemblage	Lineation	Foliation	Recrystallization mechanism	CPO	O A	RMS grain size ( $10^X(\mu\text{m})$ , range: $2\sigma$ )	Mode of logarithmic grain size ( $10^X(\mu\text{m})$ , range: $2\sigma$ )
Chlorite zone	ASM1	Quartz, Calcite, Albite, Phengite, Chlorite, Graphite	Quartz strain fringe, Elongated quartz grain	Solution seam	SGR	Crossed girdle?	N C *	XZ: 1.54 ( $\pm 0.03$ ) YZ: 1.29 ( $\pm 0.02$ )	NC
Garnet zone	ASM2	Quartz, Phengite, Albite, Garnet, Ilmenite, Rutile	Elongated quartz grain, Aligned phengite	Aligned phengite	SGR+GBM	Crossed girdle (Type 1)	43 – 47	XZ: 1.70 ( $\pm 0.11$ ) YZ: 1.42 ( $\pm 0.12$ )	XZ: 1.93 ( $\pm 0.03$ ) YZ: 1.75 ( $\pm 0.03$ )
Albite-biotite zone	ASM3	Quartz, Phengite, Albite, Piemontite, Ilmenite, Rutile	Not observed	Aligned phengite	SGR+GBM	Crossed girdle (Type 1)	48 – 64	PZ**: 1.46 ( $\pm 0.09$ )	PZ: 1.67 ( $\pm 0.11$ )
Albite-biotite zone	ASM4	Quartz, Phengite, Albite, Ilmenite, Rutile	Not observed	Aligned phengite	SGR	Small girdle	46 – 49	PZ: 1.37 ( $\pm 0.07$ )	NC
Albite-biotite zone	ASM5	Quartz, Phengite,	Not observed	Phengite shear band	BLG	Small girdle	37 – 42	PZ: 1.54 ( $\pm 0.03$ )	NC

\* Not calculated

\*\* Plane parallel to Z axis



**Table2 Deformation temperature of samples**

Sample No.	Metamorphic zonation	Deformation temperature (°C)
ASM1	Chlorite zone	NC
ASM2	Garnet zone	344–376
ASM3	Albite-biotite zone	384–512
ASM4	Albite-biotite zone	368–392
ASM5	Albite-biotite zone	296–336

NC: Not calculated

**Table 3 Differential stress estimated by piezometer**

(Cr: Cross et al., 2017; Cr+Ho: Cross et al., 2017 corrected by Holyoke, 2010; Sh: Shimizu, 2012)

	Differential Stress in uniaxial condition (MPa)			Differential stress in plane stress condition (MPa)		
	Cr	Cr+Ho	Sh	Cr	Cr+Ho	Sh
ASM1 (XZ)	47.6	34.7	NC	55.0	40.1	NC
ASM1 (YZ)	71.7	52.3	NC	82.8	60.4	NC
ASM2 (XZ)	36.9	26.9	46.5	42.6	31.1	53.7
ASM2 (YZ)	58.3	42.6	65.9	67.3	49.1	76.1
ASM3 (PZ)	54.6	39.9	60.7	63.0	46.0	70.1
ASM4 (PZ)	62.9	45.9	NC	72.6	53.0	NC
ASM5 (PZ)	110.1	80.4	NC	127.1	92.8	NC

NC: Not calculated

305

310



## 4 Discussion

### 315 4.1 Stress recorded by quartz microstructure and in the subduction plate interface

In this section, we discuss the relationship between the stress recorded by the quartz microstructure and the stress state along the subduction interface. In this contribution, we use the term stress to refer to differential stress and shear stress. In Appendix B, we also refer to the tensor nature of stress including the deviatoric stress. For the stress estimates, we focused on the microstructures of samples ASM1–5.

320 In sample ASM1, quartz veins in the rock body were analyzed, and the possibility that the estimated stress is not representative of the stress experienced by the larger-scale rock body needs to be considered. In contrast to the quartz veins, the surrounding rock body shows microstructures indicative of deformation by pressure solution creep (Fig. 6a). However, parts of the quartz fringe have undergone recrystallization and these domains show very similar recrystallized quartz grain size to that of the recrystallized quartz vein (Fig. 6a, 6b) indicating multiple domains within the rock were deformed under the same stress.  
325 Therefore, it is concluded that the stress estimated from sample ASM1 is representative of the stress of the whole rock body around the location ASM1.

In Sample ASM2–4, in addition to quartz (volume fraction 70–80%: inferred by indexing rate of EBSD analysis), albite and phengite are also significant mineral components (Fig. 6c–6f). Albite includes traces of a  $D_r$  foliation oblique to the external  $D_s$  foliation which is partly defined by the alignment of phengite. These observations suggest that both albite and phengite  
330 were formed before or synchronously with  $D_s$ , the timing of quartz deformation. This implies that albite and phengite have both been deformed along with the quartz. However, in albite, wavy extinction is weak and not nearly as well developed as in quartz (e.g., albite in Fig. 6d), suggesting that the albite underwent only very limited intracrystalline deformation during the  $D_s$  deformation. In general, albite is known to have a higher yield strength than quartz in this temperature condition (Passchier & Trouw, 1996), in agreement with the above assumption. A muscovite flow law (Mariani et al., 2006) suggests that the strain  
335

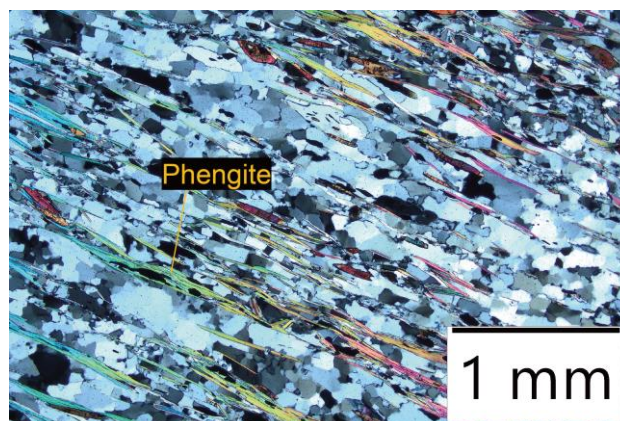


**Figure 8: Microstructure of phengite in quartz schist (sample ASM3). Phengite (greenish to purplish interference colored platy mineral) does not form a continuous foliation longer than a few mm.**





rate of phengite should be 10 times higher than that of quartz. However, phengite in this sample hardly forms a continuous  
340 foliation (Fig. 6e, 6f, 8), which means that deformation is unlikely to propagate. It has been suggested that in such a structure,  
quartz is distributed in a mesh-like pattern and supports almost all of the stress applied to the rock—an interconnected network  
(Alaoui et al., 2022). Assuming that this situation applies in samples ASM2–4, the quartz deformation can be regarded as  
representative of the deformation of the rock body around samples ASM2–4. Therefore, the stress recorded by the quartz in  
samples ASM2–4 is considered to be representative of the stress recorded by the rock body around samples ASM2–4.

345 There are mafic schist domains around the pelitic, psammitic, and quartz schists, in which samples ASM1–4 were collected.  
Mafic schist contains only small amounts of quartz and it is reasonable that the physical characteristic of mafic schist is  
different from that of pelitic and quartz schists. Different strain rates are expected in such heterogenous domains even if the  
stress is homogenous. However, in this field area the fraction of mafic schist is small (Fig. 3), and irrespective of the stress  
distribution, we consider that the effect of mafic schists on the deformation of rocks along the subduction plate interface in the  
350 present case can be safely ignored. Therefore, we conclude that the stresses inferred from our samples are representative of the  
stresses on a larger scale and along the subduction zone plate interface where the Sanbagawa belt was formed.

Shear bands were observed in sample ASM5 (Fig. 6g, 6h). The formation of shear bands represents local strain partitioning.  
However, sample ASM5 shows clearly low deformation temperature compared with peak metamorphic temperatures, and  
therefore it could represent the later stage deformation compared to samples ASM1–4. (Sect. 4.4).

#### 355 4.2 Tectonic stage of sample deformation

Knowledge of the tectonic stage represented by the deformation recorded in the quartz samples is important when discussing  
how the stress data for individual samples can be related to stresses in the paleo-subduction plate interface. In this study, we  
first compared peak metamorphic temperatures estimated by the Raman carbonaceous material geothermometer (Kouketsu et  
al., 2021) with deformation temperatures estimated by the quartz c-axis fabric opening-angle thermometer. The P–T path of  
360 the region has been determined in previous studies and this path allows us to link the deformation temperature to pressure and  
hence depth. The retrograde P/T gradient is the most important and this has been estimated as 0.3 GPa/100°C in the albite-  
biotite zone and 0.4 GPa/100°C in the garnet and chlorite zones (Fig. 6d and 6f in Okamoto and Toriumi, 2005).

In sample ASM1, the crystallographic preferred orientation pattern fabric is not clear and the OA could not be measured.  
However, sample ASM1 records Ds deformation and recrystallized grains formed by SGR, indicating that its deformation  
365 process is dislocation creep and deformation temperature is at least about 300°C (Passchier & Trouw, 2005). This temperature  
is close to the peak temperature of about 330°C and in the following discussion, we take the deformation temperature of sample  
ASM1 to be 300–330°C.

To allow a better regional comparison between the deformation temperature and metamorphic peak temperature we also  
examined quartz fabric data from previous studies (Sakakibara et al., 1992; Wallis et al., 1992; Tagami & Takeshita, 1998;  
370 Yagi & Takeshita, 2002) that were suitable for the quartz c-axis fabric opening-angle thermometer. In many of the previous  
studies, the main ductile deformation of the region is referred to as D1 (Tagami and Takeshita, 1998; Yagi and Takeshita,

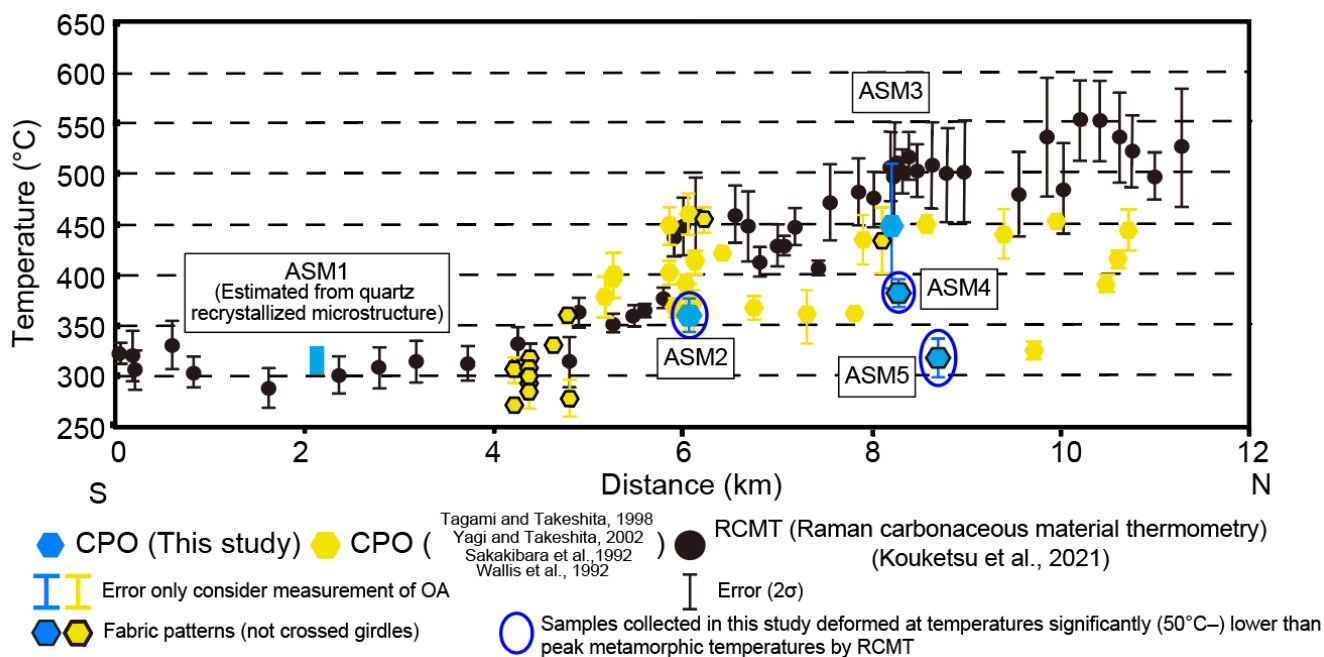


**Figure 9: A comparison between estimated peak metamorphic temperatures by the Raman carbonaceous material geothermometer (black circles), and the estimated deformation temperatures by the quartz c-axis fabric opening-angle thermometer (hexagons). The black frames around some hexagons indicate that the corresponding c-axis fabric patterns are not crossed girdles. Especially, at the higher temperature side (North of sample ASM2), all hexagons with black frames (3 samples) show small girdles, which may cause a small overestimation of the deformation temperature (Law, 2014). Blue hexagons indicate samples collected in this study. Blue circles around blue hexagons indicate these samples deformed at temperatures significantly (50°C–) lower than the surrounding peak metamorphic temperatures and may record deformation at shallower levels. Errors for the RCMT estimates are given at the 2 $\sigma$  level. Errors for the quartz c-axis fabric opening-angle thermometer are based on the measurement of OA (treated as 2 $\sigma$ ). The deformation temperature for sample ASM1 (blue rectangle) is derived from microstructural observations.**

2002). D1 has the same characteristics as Ds in this study and the same reference frame of the X-axis and XY plane was used to plot the quartz fabric as used in this study so a direct comparison is possible. One previous study (Sakakibara et al., 1992) relates the deformation of the study area to an Sb<sub>2-2</sub> deformation phase. The Sb<sub>2-2</sub> is defined by coupling of the Saruta-Fuyunose-Sogauchi units (classified as the Shirataki unit in this study) and the Sakamoto unit (classified as the Shirataki and Oboke unit in this study). We consider it to be the same as the Ds deformation because the boundary between the Shirataki unit which is referred to as the Saruta-Fuyunose-Sogauchi units and the Oboke unit which is referred to as the Sakamoto unit contains a mixed domain with rocks derived from both the overlying Shirataki and underlying Oboke units, in which



characteristics of the Ds deformation were observed (Aoya et al., 2017). Measured OA from previous studies were shown in Appendix A.

It is clarified that most of the plotted data are within a few tens of degrees Celsius below the peak metamorphic temperature (Fig. 9). However, some samples, mainly in the high metamorphic region, show deformation temperatures that are clearly lower than the peak metamorphic temperature (blue circles). It is assumed that samples ASM 1 and 3 were deformed near the peak metamorphic temperatures, samples ASM 2 and 4 were deformed at the early stage of exhumation, and sample ASM5 was deformed at the late stage of exhumation. We used samples ASM1–4 in the next discussion. Estimates for the pressures at which samples ASM1 and 3 were deformed are about  $0.55\pm 0.1$  GPa (21 km) and  $0.7\pm 0.2$  GPa (27 km). Samples ASM2 and 4 were deformed at  $0.45\pm 0.1$  GPa (17 km) and  $0.5\pm 0.1$  GPa (19 km). The error of estimated pressure condition is derived from the measurement error of OA (treated as  $2\sigma$ ) and RCMT ( $2\sigma$ ), and the range of pressure condition (Enami et al., 2014: treat as  $2\sigma$ ).

#### 4.3 Spatial distribution of stress in the Sanbagawa subduction zone and relationship with deep slow earthquakes

The use of different proposed piezometer relationships based on grain size results in significant differences in the estimated stress. A further complication highlighted by this study is the variation in grain size depending on the orientation of the observed section with respect to the finite strain axes. This issue is not significant in deformation experiments that predominantly use uniaxial shortening but is significant in natural samples that are close to plane strain. When these uncertainties are included, the differential (shear) stress was found to be 31.1–82.8 MPa (15.5–41.4 MPa) for plane stress, in samples ASM1–4. Moreover, there was no clear correlation between the sample location and stress (Fig. 10) implying stress was constant throughout the range of different temperatures and pressures during peak metamorphism to the early stage of exhumation. This suggests that constant stress regardless of depth was maintained over a long timescale. If the stress recorded by the quartz recrystallization is representative of the stress along the plate interface, this result indicates that the stress along the former plate interface was independent of depth and nearly constant over the depth range of 17–27 km where depth is calculated under the assumption that granitic rock is present up to a depth of 20 km, and gabbroic rock is present at greater depths (e.g., Aoya et al., 2013a). This information can be applicable to long-timescale subduction zone modelling.

In an earlier study, Takeshita (2021) reports the results of microstructural analyses of quartz-rich samples in the Shirataki unit of the Sanbagawa belt and estimated differential stress from quartz grain size. Takeshita (2021) proposes a decrease in differential stress with increasing structural level (“Upper Chl” to “Ab-bt” of Fig.6 in Takeshita, 2021), which corresponds to increasing metamorphic temperature and pressure in this study domain. The results of Takeshita (2021) differ from those of this study, and it is particularly clear that samples formed by SGR+GBM (GBM in Takeshita, 2021) show very low differential stress.

This difference may be mainly attributed to the type of piezometer used to analyze the recrystallized microstructures formed by SGR+GBM. As mentioned above, the recrystallized microstructure formed by SGR+GBM is developed by the formation

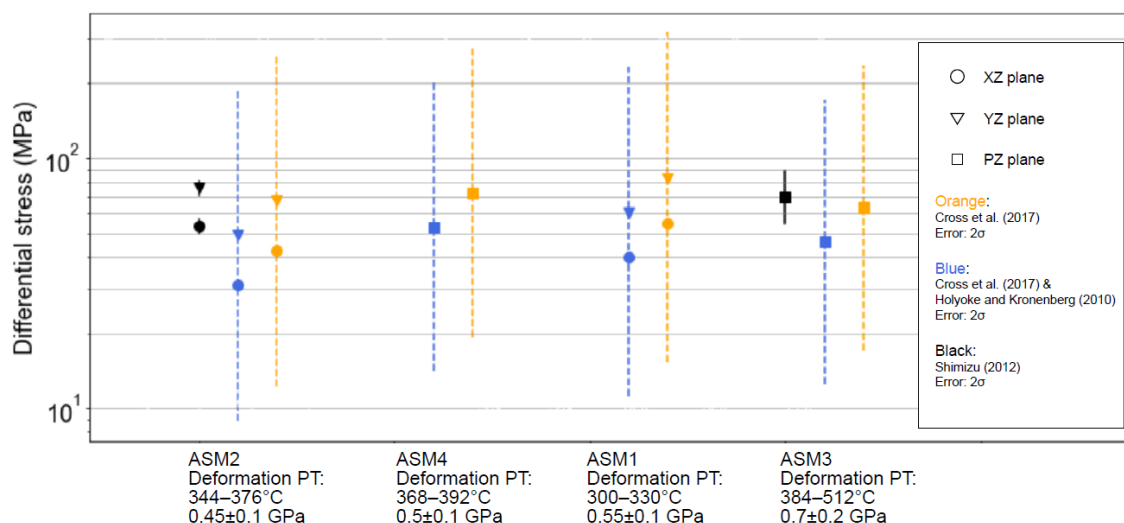
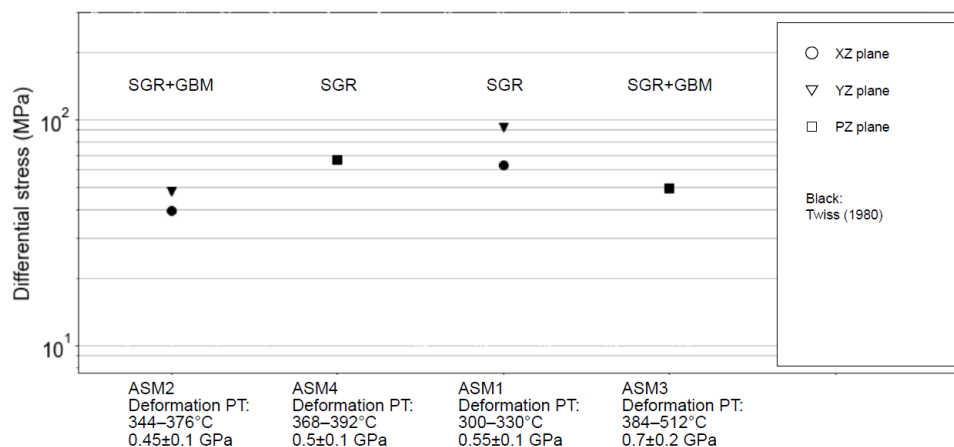


**Figure 10: Differential stress for plane stress conditions estimated using piezometers based on recrystallized quartz grain size. The vertical axis indicates differential stress. Black points were calculated following Shimizu (2012), orange points were calculated following Cross et al. (2017), and blue points were calculated following Cross et al. (2017) using a correction for measured values by Griggs apparatus, which is proposed by Holyoke and Kronenberg (2010). Circle, triangle, and square points indicate measurements in the XZ, YZ, and PZ planes. The black, orange, and blue lines show uncertainties associated with differential stress associated with the black, orange, and blue points ( $2\sigma$ ).**

425  
430

of subgrains by SGR and the migration of grain boundaries by GBM. Several studies have pointed out that dislocation movement and grain nucleation have a greater temperature dependence than grain boundary migration and this leads to a grain size decreases with increasing temperature for the same differential stress (e.g. De Bresser, 1998; Shimizu, 1998) (and greater strain rate). Furthermore, Shimizu (2008, 2012) theoretically derived a piezometer for the SGR+GBM recrystallized microstructure that incorporates this temperature effect and shows a grain size decreases with increasing deformation temperature for the same differential stress. In contrast, Takeshita (2021) uses a piezometer proposed by Twiss (1980), in which grain size is temperature independent (details of the differences between the theories of Twiss (1980) and Shimizu (2008, 2012) are described in Shimizu (2008)). Twiss (1980) quoted data from various experimental studies in which dynamically recrystallized grain size and differential stress were determined by using recrystallized microstructure of experimental samples and natural samples, including quartz, olivine, and metal alloys. Twiss (1980) subsequently generated the non-dimensional piezometer that best fits these experimental data (equation 23 in Twiss (1980)), and Takeshita (2021) applied quartz physical property data (Table 2 in Twiss (1980)) to this non-dimensional piezometer. This non-dimensional piezometer does not have a strong material dependency and it is reasonable to use experimental results for different materials to construct a piezometer. However, a potentially significant problem is that the deformation experiments used in Twiss (1980)

435  
440



445

**Figure 11: Differential stress for plane stress conditions estimated using piezometers by Twiss (1980). The vertical axis indicates differential stress. Stress estimated by microstructures formed by SGR+GBM is clearly lower than stress estimated by microstructures formed by SGR.**

450

were conducted under higher temperature conditions (814–1699°C) than the deformation temperatures of the samples in the Sanbagawa belt (about 500°C). If SGR+GBM microtextures are contained in these deformation experiments, the piezometer shows smaller grain size under the same stress condition and therefore underestimates the differential stress when analyzing recrystallized microstructure formed by SGR+GBM in the Sanbagawa belt. We note that this problem also exists in the piezometer proposed by Cross et al. (2017), but this piezometer is based on analysis of newly recrystallized grains alone and the size of these grains is only weakly affected by GBM, so the temperature effect should be relatively small. The result of stress estimation of samples ASM1–4 by using the piezometer of Twiss (1980), which shows lower differential stress values for microstructures formed by SGR+GBM, and higher values for microstructures formed by SGR (Fig. 11), supports this idea.

455

The other possibility is a selection of microstructure. In Takeshita (2021), especially in samples from higher metamorphic grade zone, some grain size data whose value is small is considered “overprinting”, and excluded from stress estimation (Fig. 3 in Takeshita, 2021). It is possible that quartz microstructures like our samples were excluded, and microstructures with relatively large grain size were selected to stress estimation, resulting in decreasing stress trend.

460

465

The Sanbagawa belt formed in a relatively warm subduction zone, and deep slow earthquakes are commonly observed in modern-day warm subduction zones such as SW Japan (Obara, 2020) which has a similar thermal structure to the Sanbagawa belt (Fig. 2). Moreover, the depth of deformation of samples ASM1–3 is consistent with the depth at which deep slow earthquakes occur. Deep slow earthquakes are commonly observed concentrated in a domain near and updip of the mantle wedge corner (Behr and Bürgmann, 2021). In the Sanbagawa belt, it is found that ultramafic rocks of the Shirataki unit are not present in the chlorite and lower garnet zone (Aoya et al., 2013a) and it is concluded that these ultramafic rocks are derived from the mantle wedge (Aoya et al., 2013a; Aoya and Endo, 2017). The peak pressure of the garnet zone corresponds to a depth of approximately 30–35 km, indicating that the mantle wedge of the Sanbagawa subduction zone was located at depths



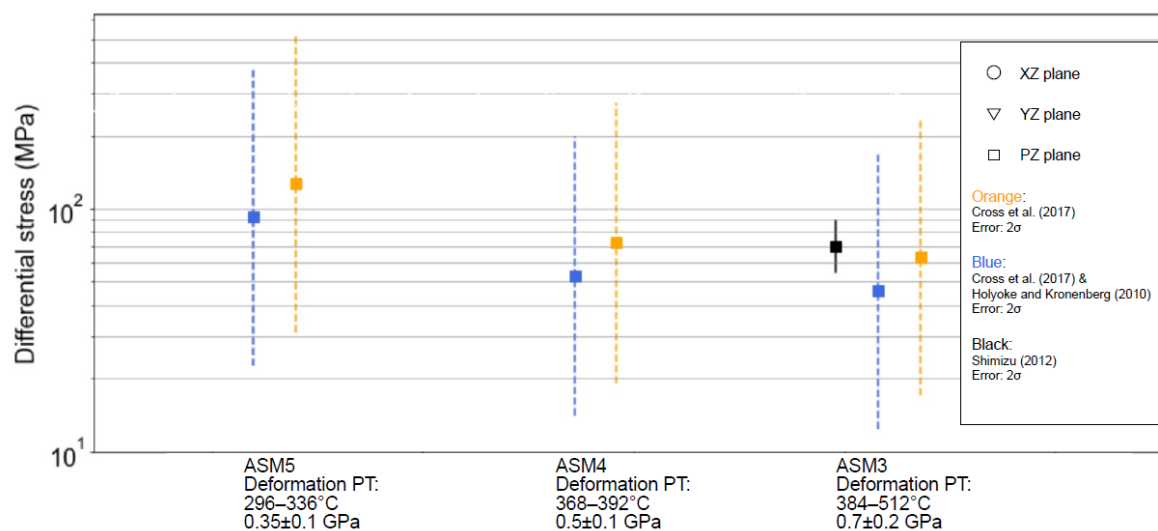
470 deeper than 30–35 km. The paleodepths of samples ASM1–4 were 17–27 km, which is near and updip of the mantle wedge, suggesting that these samples were formed in a region with features similar to the deep slow earthquakes domain.

Moreover, the shear stress drop on the fault plane caused by slow earthquakes could be hundreds to thousands of times smaller than that of ordinary earthquakes (e.g., Ito and Obara, 2006; Behr and Bürgmann, 2021), and unless the fault plane is not oriented to the direction of maximum/minimum principal stress axes, it has little effect on the estimated shear stress value. 475 Therefore, the estimated stress may represent the initial conditions from which slow earthquakes in the same domain nucleated.

#### 4.4 Stress evolution of rock bodies during exhumation

In Fig. 9, the samples with blue circles are considered to have formed later in the exhumation process than the other samples. Therefore, to examine the changes in stresses received by the rocks during exhumation, we compared the estimated stresses of samples ASM3–5, which were collected from almost the same location and recorded different deformation temperatures. Using 480 the known P–T path we derived pressures for these samples of  $0.7\pm 0.2$  GPa (27 km) for ASM3,  $0.5\pm 0.1$  GPa (19 km) for ASM4, and  $0.35\pm 0.1$  GPa (13 km) for ASM5.

The results (Fig. 12) show that assuming plane stress conditions the estimated differential (shear) stress of samples ASM3 and 4 are  $46.1\text{--}70.1$  MPa ( $23.1\text{--}35.0$  MPa) and  $53.0\text{--}72.6$  MPa ( $26.5\text{--}36.3$  MPa), respectively, indicating that the stresses are



485 **Figure 12: Differential stress for plane stress condition estimated using piezometers based on recrystallized quartz grain size. The vertical axis indicates differential stress. Black points were calculated following Shimizu (2012), orange points were calculated following Cross et al. (2017), and blue points were calculated following Cross et al. (2017) using a correction for measured values by Griggs apparatus, which is proposed by Holyoke and Kronenberg (2010). Circle, 490 triangle, and square points indicate measurements in the XZ, YZ, and PZ planes. The black, orange, and blue lines show uncertainties associated with differential stress associated with the black, orange, and blue points ( $2\sigma$ ).**



almost constant until the middle part of the ascent. In contrast, the estimated differential (shear) stress of sample ASM5, which is the final recorded stage of ductile deformation during ascent in this region, was found to increase significantly, ranging from 92.8 to 127.1 MPa (46.4 to 63.6 MPa). As shown in Fig. 9, many samples recorded deformation temperatures close to the peak and therefore represent conditions close to the onset of exhumation. Therefore, it is suggested that stress conditions remained similar until mid-crustal levels where deformation became concentrated in discrete bands associated with higher stresses as represented by sample ASM5.

## 5 Conclusions

Quartz-rich rocks and quartz veins from the subduction-type Sanbagawa belt exposed in central Shikoku, Southwest Japan preserve deformation-related microstructures that can be used to estimate paleo differential (shear) stresses. These quartz-rich rocks have characteristics of quartz dominant deformation, and quartz veins record the same differential (shear) stress values as surrounding rocks, suggesting that the results are representative for the subduction interface. Estimates of both differential (shear) stress and deformation temperature were obtained from measurements of recrystallized grain sizes and the opening angle of quartz c-axis fabric patterns. The known P–T paths for the region can be used to relate temperature to pressure (and depth). After correcting the differential (shear) stress estimates based on uniaxial compression deformation experiments to account for plane stress conditions, the obtained results show differential (shear) stresses of 31.1–82.8 MPa (15.5–41.4 MPa) consistent over depths of 17–27 km in the paleo subduction channel. Differential (shear) stresses during exhumation initially show little change but increase during the lower T final stages of exhumation-related ductile deformation. The prograde P–T path of the Sanbagawa belt is similar to the thermal structure modelled for modern-day warm subduction zones such as SW Japan where deep slow earthquakes are common. Some of the studied samples were derived from depths near the mantle wedge where deep slow earthquakes are common. Therefore, the estimated differential (shear) stress may not only be useful to long-timescale subduction zone modelling but also represent the initial conditions from which slow earthquakes in the same domain nucleated.

515

520



## Appendices

### 525 Appendix A: Measured OA from c-axis fabric patterns by previous studies.

**Table A1 the results of quartz c-axis fabric opening-angle measurement**

Sample No.	Metamorphic zonation	Fabric pattern	OA(°)	Deformation temperature (°C)
Sakakibara et al., 1992				
C	Ol-Bt	Type	51–53	408–424
D	Ol-Bt	Type I	48–50	384–400
E	Ol-Bt	Type I	56–57	448–456
G	Ol-Bt	Type I	52–57	416–456
K	Al-Bt	Small girdle	50–58	400–464
L	Gt	Type I	51–57	408–456
N	Gt	Type I	41–48	328–384
P	Gt	Type I	45–47	360–376
Tagami and Takeshita, 1998 (sample with small girdle were excluded)				
1	Chl	Cleft girdle	37–40	296–320
2	Chl	Cleft girdle	33–34	264–272
3	Chl	Cleft girdle	33–36	264–288
4	Chl	Cleft girdle	36–38	288–304
5	Chl	Cleft girdle	38–39	304–312
6	Chl	Cleft girdle	37–42	296–336
7	Chl	Cleft girdle	36–37	288–296
8	Chl	Cleft girdle	41–42	328–336
9	Chl	Cleft girdle	32–37	258–296
10	Chl	Cleft girdle	44–45	352–360
11	Chl	Type I	45–50	360–400
12	Chl	Type I	49–50	392–400
13	Chl	Type I	47–53	376–424
14	Chl	Type I	54–58	432–464





**Table A1 the results of quartz c-axis fabric opening-angle measurement**

Sample No.	Metamorphic zonation	Fabric pattern	OA(°)	Deformation temperature (°C)
Tagami and Takeshita, 1998 (sample with small girdle were excluded)				
15	Chl	Type I	48–52	384–416
18	Chl	Type I	45–47	360–376
23	Gt	Type I	44–48	352–384
24	Gt	Type I	48–50	384–400
25	Gt	Type I	45–47	360–376
26	Gt	Type I	43–50	344–400
27	Gt	Type I	43–48	344–384
28	Gt	Type I	47–48	376–384
29	Gt	Type I	55–60	440–480
30	Gt	Type I	50–52	400–416
31	Gt	Type I	52–53	416–424
33	Gt	Type I	52–53	424–432
Yagi and Takeshita, 2002				
T2	Ol-Bt	Type II	53–58	424–464
T4	Ab	Type I	55–57	440–456
T5	Gt	Type I	44–45	352–360
T7	Gt	Small girdle	55–58	440–464
Wallis et al., 1992				
SB19	Ol-Bt	Type I	38–39	304–312

**Appendix B: Differential (shear) stress calculation under any deviatoric stress tensor.**

530 It is the deviatoric component of the stress tensor that causes shearing of materials. In general, definition of this tensor requires knowledge of all three of its principal stresses. However, the difference between the maximum and minimum principal stresses, or differential stress, can be used as an effective measure of the stresses causing deformation. Geological piezometers are presented as equations relating this differential stress to grain size. The main piezometer used in this study (Cross et al., 2017) is based on the results of deformation experiments under uniaxial conditions ( $\sigma_1 > \sigma_2 = \sigma_3$ ). Therefore, to convert the output differential stresses to differential stresses in the stress field more representative of natural conditions ( $\sigma_1 > \sigma_2 > \sigma_3$ ), a



535 correction must be made. An overview of the procedure is given below (see also Behr and Platt., 2013). For simplicity, the material is assumed to be isotropic.

Deviatoric stress applied to a material causes it to shear and undergo strain. This strain generates elastic strain energy. The elastic strain energy due to the shear is the same amount as the elastic strain energy due to the deviatoric stress tensor the object is subjected to.

540 The relationship between the deviatoric stress tensor (or differential stress) and grain size in the piezometer can then be summarized as the relationship between the elastic strain energy to which the material is subject and the grain size. Therefore, when the deviatoric stress tensor changes, the elastic strain energy applied to the material also changes, and the grain size will be different even if the differential stress is the same.

The second invariant of the deviatoric stress tensor,  $J_2$ , is a scalar quantity that describes the magnitude of the stress tensor independent of its orientation and is given by the following equation.

$$J_2 = \frac{[\sigma_1^2 + \sigma_2^2 + \sigma_3^2 - (\sigma_1\sigma_2 + \sigma_2\sigma_3 + \sigma_3\sigma_1)]}{3} \quad (1)$$

Where  $\sigma_i$  is the magnitude of the principal stresses.

Substituting any stress condition,

$$\sigma_2 = (1 - m)\sigma_1 + m\sigma_3, \quad 0 < m < 1 \quad (2)$$

550 Eq. (1) is transformed into the following

$$J_2 = \frac{(m^2 - m + 1)(\sigma_1^2 + \sigma_3^2)}{3} \quad (3)$$

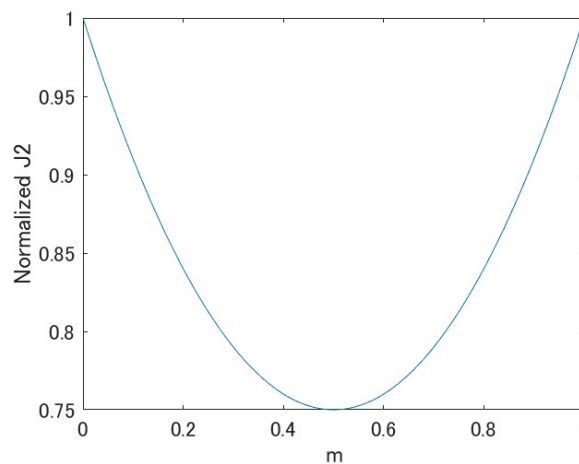


Figure B1: Value of  $J_2$  normalized by max value. The horizontal axis indicates  $m$  in the above equation. 0.5: plane stress, 0 or 1: uniaxial.



It can be seen from Eq. (3) and Fig. B1 that the elastic strain energy varies with the deviatoric stress tensor for the same differential stress: in the plane stress condition, it is 3/4 times lower than for uniaxial conditions, where it reaches a maximum value. In order to give the same strain energy, this second invariant should show the same value. Therefore, to result in the same strain energy in the natural plane stress field as that given to quartz in the uniaxial compression test, the differential stress  
560  $(\sigma_1 - \sigma_3)$  for plane stress has to be greater by a factor of  $\sqrt{\frac{4}{3}} = \frac{2}{\sqrt{3}}$ .

Since the dynamically recrystallized quartz grains measured in this study were generated in a natural stress field with conditions inferred to be close to plane stress, the original differential stress in natural conditions can be calculated by multiplying the piezometer results by  $\frac{2}{\sqrt{3}}$  to 1. Since shear stress is 0.5 times the differential stress, the shear stress can be calculated by dividing the measurement result by  $\frac{4}{\sqrt{3}}$  to 2.

565

### Appendix C: Error calculation method when using the Cross et al. (2017) piezometer

The Cross et al. (2017) piezometer can be written as follows using the Briggsian logarithm of the experimentally obtained differential stress and the Briggsian logarithm of the recrystallized grain size:

$$\log_{10}RMS = a + b\log_{10}\sigma \quad (4)$$

570 where RMS is root mean square grain size ( $\mu\text{m}$ ),  $\sigma$  is differential stress (MPa), and a, b are parameters obtained by fitting experimental data. The errors shown in the piezometer of Cross et al. (2017) are derived from parameter fitting.

When substituting the measured grain size into this piezometer, we consider the error propagation between the error of the piezometer and the measured grain size (the Briggsian logarithm of the RMS:  $\log_{10}RMS$ ). The standard error of “the mean of the squares of particle sizes” can be calculated by using the Central Limit Theorem. The Briggsian logarithm of the square  
575 root of “the mean of the squares of the particle sizes” is “ $\log_{10}RMS$ ”. Therefore, we generated 10000 random numbers following a normal distribution with the mean and standard deviation of the “mean of the squares of particle sizes” and calculated the Briggsian logarithm of the square root of the generated random numbers to obtain a random number following “ $\log_{10}RMS$ ”. By calculating the mean and standard deviation of these random numbers, the mean and standard deviation of “ $\log_{10}RMS$ ” were calculated and used as the error of the measured particle size. In this study, the code of Cross et al. (2017)  
580 was modified to perform the calculation (Code and data available).

Finally, the error in the measured particle size and the error in the piezometer were substituted into the error propagation equation. Since a and b were obtained from the same experiment, correlation coefficients were calculated.

$$f(a, b, Y) = \log_{10}\sigma = \frac{\log_{10}RMS - a}{b} \quad (5)$$



$$S_{\log_{10}\sigma} = \sqrt{\left(\frac{\partial f}{\partial a}\right)^2 s_a^2 + \left(\frac{\partial f}{\partial b}\right)^2 s_b^2 + \left(\frac{\partial f}{\partial Y}\right)^2 s_Y^2 + 2\left(\frac{\partial f}{\partial a}\right)\left(\frac{\partial f}{\partial b}\right) s_{ab}}$$

$$585 = \sqrt{\left(\frac{1}{-1.41}\right)^2 (S_{\log_{10}RMS})^2 + \left(\frac{\log_{10}RMS - 3.91}{(-1.41)^2}\right)^2 (0.21)^2 + \left(\frac{1}{-1.41}\right)^2 (0.21)^2 + 2\left(\frac{1}{-1.41}\right)\left(\frac{\log_{10}RMS - 3.91}{(-1.41)^2}\right) 0.096} \quad (6)$$

S is the standard deviation (error). Uncertainties of estimated differential (shear) stress are related to both the piezometer and the grain size measurement.

#### Appendix D: Error calculation method when using the Shimizu (2012) piezometer

The Shimizu (2012) piezometer can be written as follows using the differential stress  $\sigma$ , deformation temperature T, and the mode of the natural logarithm of the recrystallized grain size (defined as ModelnD):

$$ModelnD = \ln(9.98 \times 10^2 \times \sigma^{-1.25}) + \frac{12.4 \text{ kJmol}^{-1}}{RT} \quad (7)$$

ModelnD is measured by the probability density of logarithmic grain sizes obtained by applying kernel density estimation to the grain size histogram. Since the logarithmic grain size distribution can be regarded as the logarithmic normal distribution (Shimizu, 1998), and ModelnD is almost identical to the mean of the power index of grain size, the confidence interval of ModelnD can be calculated using the properties of a Student's t-distribution. However, the number of data is at least 72 (number of grains), indicating that Student's t-distribution closely approximates a standard normal distribution. Therefore, the standard error of ModelnD was calculated using the Central Limit Theorem. In this study, the code of Cross et al. (2017) was modified to perform the calculation (Code and data available).

The uncertainties by the piezometer of Shimizu (2012) are not shown. Therefore, uncertainties of estimated differential (shear) stresses are only related to grain size measurement and deformation temperature.

$$S_{\log_e\sigma} = \sqrt{\left(\frac{1}{1.25}\right)^2 (S_{ModelnD})^2 + \left(\frac{1193.7}{(Deformation\ Temperature)^2}\right)^2 (S_{Deformation\ Temperature})^2} \quad (8)$$

S is the standard deviation (error).

**Code and data availability:** Code and data are available at <https://doi.org/10.5281/zenodo.8085144> (Koyama et al., 2023: <https://github.com/YukinojoKoyama/Koyama-et-al.CodeandData/tree/v1.0.0>)

**Author contributions:** YK and SWR developed the conceptualization of this study. All authors conducted geological field surveys and specimen sampling. TN and YK designed thin section production methods. TN provided the SEM-EBSD analysis method and appropriate analysis conditions. Crystallographic orientations were collected by YK and TN. Stress and deformation temperature estimation method were organized by all authors. YK was involved in the data curation and modified computer programs from previous studies. All authors were involved in the validation process. The interpretation of the dataset, preparation of the original draft, figure design, reviews, and editing of the paper were carried by all authors.



**Competing interests:** The authors declare that they have no conflict of interest.

**Acknowledgments:** We are grateful to Ken Yamaoka and Thomas Yeo of the University of Tokyo for a lot of useful advice concerning the polishment of thin sections and the deformation mechanisms of quartz. We also thank Kazuhito Ozawa, Asuka Yamaguchi, Yukio Masumoto, and all the members of the SGT and Petrotectonics seminar at the University of Tokyo for helpful discussions and suggestions on this research. People that have contributed to MTEX are also acknowledged for providing an open-source MTEX toolbox for MATLAB. This research was supported by JSPS Grants in Aid 21H05202, 21H01188 and 20KK0079 awarded to SW.

## References

- 620 Alaoui, K., Airaghi, L., Stünitz, H., Raimbourg, H., and Précigout, J.: Different mechanical behavior at the same P-T conditions in biotite-quartz assemblage: interconnectivity and composition effect of experimentally deformed mica, EGU General Assembly 2022, doi: 10.5194/egusphere-egu22-5108, 2022.
- Aoya, M.: P-T-D Path of Eclogite from the Sambagawa Belt Deduced from Combination of Petrological and Microstructural Analyses, *J. Petrol.*, 42(7), 1225–1248, 2001.
- 625 Aoya, M.: Structural position of the Seba eclogite unit in the Sambagawa Belt: Supporting evidence for an eclogite nappe, *Isl. Arc.*, 11, 91–110, doi:10.1046/j.1440-1738.2002.00359.x, 2002.
- Aoya, M. and Endo, S.: Recognition of the ‘early’ Sambagawa metamorphism and a schematic cross-section of the Late-Cretaceous Sambagawa subduction zone, *J. Geol. Soc. Japan.*, 123(9), 677–698, doi:10.5575/geosoc.2017.0008, 2017.
- Aoya, M., Noda, A., Mizuno, K., Mizukami, T., Miyachi, Y., Matsuura, H., Endo, S., Toshimitsu, S., and Aoki, M.: Geology of the Niihama District. Quadrangle Series 1:50,000, *Geol. Surv. Japan.*, AIST., 2009.
- 630 Aoya, M., Endo, S., Mizukami, T., and Wallis, S. R.: Paleo-mantle wedge preserved in the Sambagawa high-pressure: Metamorphic belt and the thickness of forearc continental crust, *Geology*, 41(4), 451–454, doi:10.1130/G33834.1, 2013a.
- Aoya, M., Noda, A., Mizuno, K., Mizukami, T., Miyachi, Y., Matsuura, H., Endo, S., Toshimitsu, and S., Aoki, M.: Geology of the Niihama District. Quadrangle Series 1:50,000, *GSJ. AIST.*, Tsukuba, 2013b.
- 635 Aoya, M., Mizukami, T., and Endo, S.: Geologic traverse of the Sambagawa metamorphic belt in central Shikoku, SW Japan, *J. Geol. Soc. Japan.*, 123(7), 491–514, Doi:10.5575/geosoc.2017.0038, 2017.
- Bachmann, F., Hielscher, R., and Schaeben, H.: Grain detection from 2d and 3d EBSD data-Specification of the MTEX algorithm, *Ultramicroscopy*, 111(12), 1720–1733, doi:10.1016/j.ultramic.2011.08.002, 2011.
- Banno, Shohei. and Sakai, Chihiro.: Geology and metamorphic evolution of the Sanbagawa metamorphic belt, Japan, *Geol. Soc. Lond. Spec. Pub.*, 43, 519–532, doi:10.1144/GSL.SP.1989.043.01.50, 1989.
- 640 Behr, W. M., and Bürgmann, R.: What’s down there? The structures, materials and environment of deep-seated slow slip and tremor, *Phil. Trans. R. Soc. A.*, 379(2193), doi.org/10.1098/rsta.2020.0218, 2021.



- Behr, W. M. and Platt, J. P.: Rheological evolution of a Mediterranean subduction complex, *J. Struct. Geol.*, 54, 136–155, doi:10.1016/j.jsg.2013.07.012, 2013.
- 645 Chang, C., McNeill, L. C., Moore, J. C., Lin, W., Conin, M., and Yamada, Y.: In situ stress state in the Nankai accretionary wedge estimated from borehole wall failures, *Geochem. Geophys. Geosy.*, 11(12), doi:10.1029/2010GC003261, 2010.
- Cross, A. J., Prior, D. J., Stipp, M., and Kidder, S.: The recrystallized grain size piezometer for quartz: An EBSD-based calibration, *Geophys. Res. Lett.*, 44(13), 6667–6674, doi:10.1002/2017GL073836, 2017.
- De Bresser, J. H. P., Peach C.J., Rejis, J. P. J., Spiers, C. J., On dynamic recrystallization during solid state flow: Effects of  
650 stress and temperature, 25(18), 3457–3460, *Geophys. Res. Lett.*, doi.org/10.1029/98GL02690, 1998.
- Derby, B.: The dependence of grain size on stress during recrystallization, *Acta. Metall. Mater.*, 39(5), 955–962, doi:10.1016/0956-7151(91)90295-C, 1991.
- Enami, M., Wallis, S. R., and Banno, Y.: Paragenesis of sodic pyroxene-bearing quartz schists: implications for the P-T history of the Sanbagawa belt, *Contrib. Mineral. Petr.*, 116, 182–198, doi:10.1007/BF00310699, 1994.
- 655 Endo, S. and Wallis, S. R.: Structural architecture and low-grade metamorphism of the Mikabu-Northern Chichibu accretionary wedge, SW Japan, *J. Metamorph. Geol.*, 35(6), 695–716, doi:10.1111/jmg.12251, 2017.
- Endo, S. and Yokoyama, S.: Geology of the Motoyama District. Quadrangle Series 1:50,000, *Geol. Soc. Japan.*, Tsukuba, 2019.
- Endo, S., Wallis, S., Hirata, T., Anczkiewicz, R., Platt, J., Thirlwall, M., and Asahara, Y.: Age and early metamorphic history  
660 of the Sanbagawa belt: Lu-Hf and P-T constraints from the Western Iratsu eclogite, *J. Metamorph. Geol.*, 27(5), 371–384. doi:10.1111/j.1525-1314.2009.00821.x, 2009.
- Endo, S., Wallis, S. R., Tsuboi, M., Aoya, M., and Uehara, S.: Slow subduction and buoyant exhumation of the Sanbagawa eclogite, *Lithos*, 146–147, 183–201. doi:10.1016/j.lithos.2012.05.010, 2012.
- Engelbreton D. C., Cox A., Gordon R. G.: Relative Motions Between Oceanic and Continental Plates in the Pacific Basin,  
665 *Geol. Soc. Am.*, doi:10.1130/SPE206-p1, 1985.
- England, P.: On Shear Stresses, Temperatures, and the Maximum Magnitudes of Earthquakes at Convergent Plate Boundaries, *J. Geophys. Res-sol. EA.*, 123(8), 7165–7202, doi:10.1029/2018JB015907, 2018.
- Faure, M.: Microtectonic evidence for eastward ductile shear in the Jurassic orogen of SW Japan, *J. Struct. Geol.*, 7(2), 175–186, doi:10.1016/0191-8141(85)90130-0, 1985.
- 670 Gao, Xiang. and Wang, Kelin.: Strength of stick-slip and creeping subduction megathrusts from heat flow observation, *Science*, 345(6200), 1038–1041, doi:10.1126/science.1255487, 2014.
- Goddard, R. M., Hansen, L. N., Wallis, D., Stipp, M., Holyoke, C. W. III, Kumamoto, K. M., and Kohlstedt, D. L.: A Subgrain-Size Piezometer Calibrated for EBSD, *Geophys. Res. Lett.*, 47(e2020GL090056), doi:10.1029/2020GL090056, 2020.
- Higashino, T.: The higher grade metamorphic zonation of the Sambagawa metamorphic belt in central Shikoku, Japan, *J.*  
675 *Metamorph. Geol.*, 8(4), 413–423, doi:10.1111/j.1525-1314.1990.tb00628.x, 1990.



- Holyoke, C. W. and Kronenberg, A. K.: Accurate differential stress measurement using the molten salt cell and solid salt assemblies in the Griggs apparatus with applications to strength, piezometers and rheology, *Tectonophysics*, 494(1–2), 17–31, [doi:10.1016/j.tecto.2010.08.001](https://doi.org/10.1016/j.tecto.2010.08.001), 2010.
- Ishii, K. and Wallis, Simon. R.: High- and low-stress subduction zones recognized in the rock record, *Earth. Planet. Sc. Lett.*, 680 531, [doi:10.1016/j.epsl.2019.115935](https://doi.org/10.1016/j.epsl.2019.115935), 2020.
- Isozaki, Y. and Itaya, T.: Chronology of Sanbagawa metamorphism. *J. Metamorph. Geol.*, 8(4), 401–411, [doi:10.1111/j.1525-1314.1990.tb00627.x](https://doi.org/10.1111/j.1525-1314.1990.tb00627.x), 1990.
- Ito, Y., Obara, K.: Very low frequency earthquakes within accretionary prisms are very low stress-drop earthquakes, *Geophys. Res. Lett.*, 33(9), [doi.org/10.1029/2006GL025883](https://doi.org/10.1029/2006GL025883), 2006.
- 685 Kouketsu, Y., Sadamoto, K., Umeda, H., Kawahara, H., Nagaya, T., Taguchi, T., Mori, H., Wallis, S., and Enami, M.: Thermal structure in subducted units from continental Moho depths in a palaeo subduction zone, the Asemigawa region of the Sanbagawa metamorphic belt, SW Japan, *J. Metamorph. Geol.*, 39(6), 727–749, [doi:10.1111/jmg.12584](https://doi.org/10.1111/jmg.12584), 2021.
- Koyama, Y., Wallis, S. R., Nagaya T.: YukinojoKoyama/Koyama-et-al.CodeandData: Code and Data (v1.0.0)., Zenodo, <https://doi.org/10.5281/zenodo.8085144>, 2023.
- 690 Kruhl, J. H.: Reply: prism- and basal-plane parallel subgrain boundaries in quartz: a microstructural geothermobarometer, *J. Metamorph. Geol.*, 16(1), 142–146, [doi:10.1111/j.1525-1314.1998.00063.x](https://doi.org/10.1111/j.1525-1314.1998.00063.x), 1998.
- Law, R. D.: Deformation thermometry based on quartz c-axis fabrics and recrystallization microstructures: A review, *J. Struct. Geol.*, 66, 129–161, [doi:10.1016/j.jsg.2014.05.023](https://doi.org/10.1016/j.jsg.2014.05.023), 2014.
- Lin, W.: Determination of in-situ stress state in a Japan Trench Fast Drilling Project (JFAST) borehole one year after the 695 Tohoku-Oki great earthquake, *International Journal of the JRCM*, 10(1), 1–4, [doi:10.11187/ijjerm.10.1](https://doi.org/10.11187/ijjerm.10.1), 2014.
- Mariani, E., Brodie, K. H., and Rutter, E. H.: Experimental deformation of muscovite shear zones at high temperatures under hydrothermal conditions and the strength of phyllosilicate-bearing faults in nature, *J. Struct. Geol.*, 28(9), 1569–1587, [doi:10.1016/j.jsg.2006.06.009](https://doi.org/10.1016/j.jsg.2006.06.009), 2006.
- Morgan, S. S. and Law, R. D.: Unusual transition in quartzite dislocation creep regimes and crystal slip systems in the aureole 700 of the Eureka Valley-Joshua Flat-Bear Creek pluton, California: A case for anhydrous conditions created by decarbonation reactions, *Tectonophysics*, 384(1–4), 209–231, [doi:10.1016/j.tecto.2004.03.016](https://doi.org/10.1016/j.tecto.2004.03.016), 2004.
- Mori, H. and Wallis, S.: Large-scale folding in the Asemi-gawa region of the Sanbagawa Belt, southwest Japan, *Isl. Arc.*, 19(2), 357–370, [doi:10.1111/j.1440-1738.2010.00713.x](https://doi.org/10.1111/j.1440-1738.2010.00713.x), 2010.
- Nagaya, T., Okamoto, A., Kido, M., Muto, J., and Wallis, S. R.: Dehydration of brucite + antigorite under mantle wedge 705 conditions: insights from the direct comparison of microstructures before and after experiments, *Contrib. Mineral. Petr.*, 177(87), [doi:10.1007/s00410-022-01956-z](https://doi.org/10.1007/s00410-022-01956-z), 2022.
- Okamoto, A. and Toriumi, M.: Progress of actinolite-forming reactions in mafic schists during retrograde metamorphism: An example from the Sanbagawa metamorphic belt in central Shikoku, Japan, *J. Metamorph. Geol.*, 23(5), 335–356, [doi:10.1111/j.1525-1314.2005.00580.x](https://doi.org/10.1111/j.1525-1314.2005.00580.x), 2005.



- 710 Okamoto, K., Shinjoe, H., Katayama, I., Terada, K., Sano, Y., and Johnson, S.: SHRIMP U-Pb zircon dating of quartz-bearing eclogite from the Sanbagawa Belt, south-west Japan: Implications for metamorphic evolution of subducted protolith, *Terra Nova.*, 16(2), 81–89, [doi:10.1111/j.1365-3121.2004.00531.x](https://doi.org/10.1111/j.1365-3121.2004.00531.x), 2004.
- Obara, K.: Characteristic activities of slow earthquakes in Japan, *P. Jpn. Acad. B-phys.*, 96(7), 297–315, [doi.org/10.2183/pjab.96.022](https://doi.org/10.2183/pjab.96.022), 2020.
- 715 Passchier, C. W. and Trouw, R. A. J.: *Microtectonics* (2nd ed.), Springer Berlin Heidelberg, Germany, 366, [doi:10.1007/3-540-29359-0](https://doi.org/10.1007/3-540-29359-0), 2005.
- Passeleque, F. X., Almakari, M., Dublanchet, P., Barras, F., Fortin, J., and Violay, M.: Initial effective stress controls the nature of earthquakes, *Nat. Commun.*, 11, 5132, [doi.org/10.1038/s41467-020-18937-0](https://doi.org/10.1038/s41467-020-18937-0), 2020.
- Sakakibara, N., Hara, I., Kanai, K., Shiota, T., Hide, K., & Paulitsch, P.: Quartz microtextures of the Sambagawa schists and their implications in convergent margin processes, *Isl. Arc.*, 1, 186–197, [doi:10.1111/j.1440-1738.1992.tb00069.x](https://doi.org/10.1111/j.1440-1738.1992.tb00069.x), 1992.
- 720 Sands, D., E.: *Introduction to Crystallography*, W.A. Benjamin Inc., ISBN 13: 9780805384734, 1969.
- Shimizu, I.: A stochastic model of grain size distribution during dynamic recrystallization, *Philos. Mag.*, 79(5), 1217–1231, [doi.org/10.1080/01418619908210357](https://doi.org/10.1080/01418619908210357), 1998
- Shimizu, I.: Theories and applicability of grain size piezometers: The role of dynamic recrystallization mechanisms, *J. Struct. Geol.*, 30(7), 899–917, [doi:10.1016/j.jsg.2008.03.004](https://doi.org/10.1016/j.jsg.2008.03.004), 2008.
- 725 Shimizu, I.: Steady-State Grain Size in Dynamic Recrystallization of Minerals, in: *Recrystallization*, edited by Sztwiertnia, K., Intech, 371–386, [doi:10.5772/33701](https://doi.org/10.5772/33701), 2012.
- Stipp, M. and Tullis, J.: The recrystallized grain size piezometer for quartz, *Geophys. Res. Lett.*, 30(21), <https://doi.org/10.1029/2003GL018444>, 2003.
- 730 Stipp, M., Stünitz, H., Heilbronner, R., and Schmid, S. M.: The eastern Tonale fault zone: A “natural laboratory” for crystal plastic deformation of quartz over a temperature range from 250 to 700 °C, *J. Struct. Geol.*, 24(12), 1861–1884, [doi:10.1016/S0191-8141\(02\)00035-4](https://doi.org/10.1016/S0191-8141(02)00035-4), 2002.
- Tagami, M. and Takeshita, T.: c-Axis fabrics and microstructures in quartz schist from the Sambagawa metamorphic belt, central Shikoku, Japan, *J. Struct. Geol.*, 20(11), 1549–1568, [doi:10.1016/S0191-8141\(98\)00044-3](https://doi.org/10.1016/S0191-8141(98)00044-3), 1998.
- 735 Takeshita, T.: Quartz microstructures from the sambagawa metamorphic rocks, southwest japan: Indicators of deformation conditions during exhumation, *Minerals-basel.*, 11(1038), <https://doi.org/10.3390/min11101038>, 2021.
- Twiss, R. J.: Theory and Applicability of a Recrystallized Grain Size Paleopiezometer, *Pageoph*, 115, 227–244, [doi:10.1007/BF01637105](https://doi.org/10.1007/BF01637105), 1977.
- Twiss, R. J.: Static theory of size variation with stress for subgrains and dynamically recrystallized grains, in: *Proceeding of conference IX. Magnitude of deviatoric stress in the earth’s crust and upper mantle*, U.S. Department of The Interior, Menlo Park, California, America, 665-683, [doi: 10.3133/ofr80625](https://doi.org/10.3133/ofr80625), 1980.
- 740





- Vavryčuk, V.: Earthquake Mechanisms and Stress Field, in: Encyclopedia of Earthquake Engineering, edited by: Beer, M., Kougoumtzoglou, I.A., Patelli, E., and Au, S-K., Springer, Berlin, Heidelberg, Germany, 728-746, doi:10.1007/978-3-642-35344-4, 2015.
- 745 Wallis, S. R.: The timing of folding and stretching in the Sambagawa belt: The Asemigawa region, central Shikoku, J. Geol. Soc. Japan., 96(5), 345–352, doi:10.5575/geosoc.96.345, 1990.
- Wallis, S. R.: Vorticity analysis in a metachert from the Sanbagawa Belt, SW Japan, J. Struct. Geol., 14(3), 271–280, doi:10.1016/0191-8141(92)90085-B, 1992.
- Wallis, S.: Exhuming the Sanbagawa metamorphic belt: the importance of tectonic discontinuities, J. Struct. Geol., 16, 83-95, 750 1998.
- Wallis, S. R., Banno, S., and Radvanec, M.: Kinematics, structure and relationship to metamorphism of the east-west flow in the Sanbagawa Belt, southwest Japan, Isl. Arc., 1(1), 176–185, doi:10.1111/j.1440-1738.1992.tb00068.x, 1992.
- Wallis, S. R., Anczkiewicz, R., Endo, S., Aoya, M., Platt, J. P., Thirlwall, M., and Hirata, T.: Plate movements, ductile deformation and geochronology of the Sanbagawa belt, SW Japan: Tectonic significance of 89-88 Ma Lu-Hf eclogite ages, 755 J. Metamorph. Geol., 27(2), 93–105, <https://doi.org/10.1111/j.1525-1314.2008.00806.x>, 2009.
- Yagi, K. and Takeshita, T.: Regional variation in exhumation and strain rate of the high-pressure Sambagawa metamorphic rocks in central Shikoku, south-west Japan, J. Metamorph. Geol., 20, 633–647, doi:10.5575/geosoc.112.S101, 2002.
- Yoshida, K., Hasegawa, A., and Okada, T.: Spatial variation of stress orientations in NE Japan revealed by dense seismic observations, Tectonophysics, 647–648, 63–72, doi:10.1016/j.tecto.2015.02.013, 2015.
- 760 Yoshioka, S., Murakami, K.: Temperature distribution of the upper surface of the subducted Philippine Sea Plate along the Nankai Trough, southwest Japan, from a three-dimensional subduction model: relation to large interplate and low-frequency earthquakes, Geophys. J. Int., 171(1), 302–315, doi:10.1111/j.1365-246X.2007.03510.x, 2007.